Accepted Manuscript

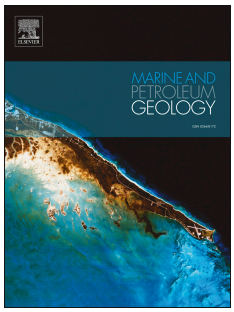

Spatial and dimensional relationships of submarine slope architectural elements: A seismic-scale analysis from the Espírito Santo Basin (SE Brazil)

Davide Gamboa, Tiago M. Alves

PII: S0264-8172(15)00067-7

DOI: 10.1016/j.marpetgeo.2015.02.035

Reference: JMPG 2167

To appear in: *Marine and Petroleum Geology*

Received Date: 16 October 2013

Revised Date: 15 February 2015

Accepted Date: 18 February 2015

Please cite this article as: Gamboa, D., Alves, T.M., Spatial and dimensional relationships of submarine slope architectural elements: A seismic-scale analysis from the Espírito Santo Basin (SE Brazil), *Marine and Petroleum Geology* (2015), doi: 10.1016/j.marpetgeo.2015.02.035.

Spatial and dimensional relationships of submarine slope architectural elements: A seismic-scale analysis from the Espírito Santo Basin (SE Brazil)

Davide Gamboa*, Tiago M. Alves

3D Seismic Lab, School of Earth and Ocean Sciences, Cardiff University, Main Building Park Place, Cardiff, CF10 3YE, United Kingdom

*Corresponding Author: GamboaDA1@cf.ac.uk

Abstract

High-quality 3D seismic data are used to interpret the styles and scale-relationships of architectural elements on the continental slope of Espírito Santo (SE Brazil). Sand-prone architectural elements identified in this work include: a) axial canyons incising a salt-withdrawal basin (Unit 1), b) turbidite lobes intercalated with heterogeneous mass-transport deposits (Unit 2), and c) channel complexes confined by salt-controlled topography (Unit 3). Analyses of width/height (W/H) ratios reveal two distinct dimensional groups: Mass-transport deposits and turbidite lobes with W/H ratios ≥ 100, and channels and blocks with W/H ratios between 1 and 30. Importantly, all buried submarine canyons and channels systems show average W/H ratios of 12-13 for different stratigraphic units. Length-width (L/W) ratios of structural and stratigraphic compartments vary between 1 and 10. A significant result of this work is the confirmation that distributions and dimensions of architectural elements can be controlled by salt-related faults and topography, with higher dimensional variability and lower continuity of sand-prone elements occurring in the vicinity of salt ridges. Our data also shows a marked tendency for clustering, and scale overlaps, between distinct architectural elements. The approach in this paper is relevant for

hydrocarbon exploration as it uses quantitative data to predict slope compartmentalisation as a function of basin geometry.

Keywords: Continental margins, SE Brazil, salt diapirs, submarine channels, mass-transport deposits, faults, compartmentalisation

1. Introduction

The Espírito Santo Basin (SE Brazil) shares a similar geological history to the Santos and Campos basins, recording significant hydrocarbon discoveries in Cretaceous, Eocene-Oligocene and Miocene strata (Bruhn and Walker, 1997; De Gasperi and Catuneanu, 2014; Fiduk et al., 2004; Moraes et al., 2006). Another common character to the three sedimentary basins is the influence halokinesis reveals on their tectonic and stratigraphic evolutions. The growth of salt structures plays a key role in controlling the distribution slope depocentres and the geometry of sand-prone strata (Alves et al., 2009; Davison, 1999; Fiduk et al., 2004; Mohriak et al., 1995; Moraes et al., 2006). In the Espírito Santo Basin, as in many other salt-rich sedimentary basins, the distribution and continuity of reservoir-prone strata depends on the spatial relationship and dimensions of salt structures, their influence on sediment flow paths and the deformation styles imposed on adjacent stratigraphic units (Clark and Cartwright, 2009; Mayall et al., 2010; Pilcher et al., 2011; Prather, 2003; Smith, 2004).

Continental margins distinct from SE Brazil's reveal a close relationship between sand-prone architectural elements and less permeable strata (Mutti and Normark, 1991; Prather et al., 2000; Slatt, 2006). Architectural elements in these regions consist of genetically related bodies with characteristic boundaries, accumulated in a common setting, and forming the fundamental building blocks of stratigraphic units (Mutti and Normark, 1991; Pyles, 2007; Slatt et al., 2009). Sand-prone architectural elements have distinctive geometries and facies compositions, and are organised in a range of dimensional hierarchies that cover various scales (McHargue et al., 2011; Mutti and Normark, 1991; Prather et al., 2000). Seismic data is commonly used to analyse the low hierarchic orders of architectural elements, namely: a) large scale stratigraphic heterogeneities separating distinct parasequences, usually 1000’s of metres wide and 100’s of metres thick, and b) medium scale inter-and intra-sandbody heterogeneities that are 100’s of metres wide and 10’s of metres thick (Ainsworth, 2010; Lasseter et al., 1986).

This study presents a 3D seismic analysis and quantification of slope architectural elements in three stratigraphic units from the Espírito Santo Basin (ESB), SE Brazil (Fig. 1). We undertook detailed measurements of architectural elements identified as sand-prone, assessing their sizes and relative distribution on a continental slope deformed by Cenozoic halokinesis.

The paper starts with a description of the geological setting of the ESB, followed by a description of the methods used. A seismic-stratigraphic characterisation of the three interpreted units precedes the quantitative analysis of architectural elements. At the end of the paper we discuss the scales of the interpreted architectural elements, and how the distribution of channels, turbidite lobes and mass-transport deposits controls the degree of continuity and connectivity of sand-prone strata. In essence, this paper addresses the following research questions:

a) How do salt diapirs influence the distribution, continuity and dimensions of sand-prone architectural elements on continental slopes?
b) Can comparable scale-relationships be established for distinct slope architectural elements?

As shown later, the study area shows a strong tendency for clustering between architectural elements, with their scales overlapping significantly within continental slope depocentres.

2. Geological Setting

2.1. Tectono-stratigraphic evolution of the Espírito Santo Basin

The Espírito Santo Basin (ESB) comprises a Mesozoic rift basin located on the SE Brazilian Margin (Fig. 1a). It is delimited by the volcanic Abrolhos Bank to the north and by the Campos Basin to the south. In the ESB, Late Berriasian to Early Aptian rifting was marked by intense tectonic activity and opening of fault-bounded extensional basins (Demercian et al., 1993; França et al., 2007; Mohriak et al., 2008; Ojeda, 1982). These same basins were filled with fluvial and

lacustrine sediments, whereas carbonate units covered structural highs (Mohriak, 2003). Continental rifting was followed by an Aptian to Early Albian transitional phase that marks a shift from continental to marine depositional sequences (Fiduk et al., 2004; Mohriak, 2003). Thick evaporite sequences were deposited during the Aptian as a result of widespread brine evaporation occurring in an arid region extending from SE Brazil to West Africa (França et al., 2007; Mohriak et al., 2008).

The Late Cretaceous to Holocene drift phase is dominated by open marine strata, which are sub-divided in two main megasequences (Fiduk et al., 2004). The Early Drift transgressive megasequence is associated with the progressive deepening of the ESB. The megasequence starts with a shallow-water Albian carbonate platform and is overlain by Late Albian to Palaeocene mudstone sequences. Thick sand-rich units were accumulated from the Santonian onwards in multiple submarine canyons (Alves et al., 2009; Bruhn and Walker, 1997; Fiduk et al., 2004).

The Late Drift megasequence reflects Eocene to Holocene tectonic reactivation of inherited rift structures, and the uplift of hinterland sediment sources. This latter event led to a widespread sea-level drop in SE Brazil, recorded in the form of a mid-Eocene regional unconformity (Cobbold et al., 2001; Demercian et al., 1993; Fainstein and Summerhayes, 1982; França et al., 2007; Mohriak, 2003; Sobreira and França, 2005). The Eocene regression is also associated with important magmatic activity, which spans the early/mid Eocene and Oligocene. Magmatism in the ESB is recorded by the development of the Abrolhos Bank, a shallow volcanic plateau with c. 30,000 km^2 (Fainstein and Summerhayes, 1982; Mohriak, 2003; Sobreira and França, 2005) (Fig. 1a). During the emplacement of the Abrolhos Bank, sediment was chiefly transported to the continental slope by submarine canyon-channel systems, accumulating as submarine fans in diapir-bounded depocentres (Bruhn and Walker, 1997; França et al., 2007). Submarine mass-wasting also played an important role in controlling the stratigraphic architecture of the Espírito Santo Basin after the Eocene, namely in the form of recurrent MTDs separating distinct turbidite intervals (Alves, 2010; Fiduk et al., 2004; Gamboa et al., 2010; Omosanya and Alves, 2013).

In the ESB, Late Drift tectonic movements were accompanied by thin-skinned gravitational gliding of Cretaceous-Cenozoic overburden units above Aptian evaporites (Demercian et al., 1983: Fiduk et al., 2004). As a result, three tectonic domains where established on the continental margin of Espírito Santo (Fig. 2a). Structures in the (proximal) extensional domain include salt rollers, salt walls, turtle anticlines and rafts (Alves, 2012; Mohriak et al., 2008; Mohriak et al., 2012). These structures change into salt diapirs in a transitional mid-slope domain. A compressional domain occurs on the distal continental slope, where allochthonous salt canopies and overhangs are observed (Davison, 2007; Demercian et al., 1993; Fiduk et al., 2004). On a local scale, halokinesis generated (confined) sediment fairways for turbidites and Cenozoic submarine channels (Alves et al., 2009; Gamboa et al., 2012b; Love et al., 2005) (Fig. 2b). Modern depositional systems include the Rio Doce Canyon System, smaller submarine channels and wide regions of mass-wasting on the continental slope (Fig. 1b).

2.2. Local setting

This study area is located at the northeast limit of the ESB (Fig. 1). The interpreted seismic volume is bounded by the Abrolhos Bank to the north, gradually deepening towards the southeast into water depths exceeding 1800 m. Present-day bathymetry reveals the growth of two northwest-trending salt ridges into which seven salt diapirs are rooted (Gamboa et al., 2011) (Fig. 2b). The western salt ridge comprises five diapirs with diameters between 3 and 6 km (D1 to D5, Figure 1b). The eastern ridge shows a relatively small salt diapir (D6) and a 14 km long salt structure (D7) (Fig 2b). The salt ridges delimit a 11 km to 20 km wide salt-withdrawal basin (Fig. 1b).

3. Methods

The interpreted 3D seismic volume covers 1670 km^2 of the ESB, in water depths ranging from 100 m to 1800 m (Fig. 1b). A dual airgun array and six 5700 m long streamers were used during

seismic acquisition. The signal was sampled at 2 ms and zero-phased migrated within 12.5-m bins. The vertical extent of the survey is limited to a time depth of 4 s two-way travel time (twtt).

The interpretation and relative dating of seismic-stratigraphic units was based on Alves et al. (2009), Fiduk et al. (2004) and Gamboa et al. (2012b). Time-depth conversions were attained using seismic velocities estimated at DSDP Site 516 (Barker et al., 1983). P-wave velocities of 1800 m/s, 2100 m/s and 3100 m/s were considered for the Miocene-Holocene, Eocene-Oligocene and Palaeogene intervals, respectively. Having these values in mind, and a dominant seismic frequency of 40 Hz for the interpreted volume, a vertical resolution of 11 m is expected for Miocene-Holocene strata; increasing to 19 m in Palaeogene units.

Thickness measurements are based on the analysis of vertical seismic sections. This information is complemented by seismic attributes such as RMS amplitude, maximum amplitude and seismic coherence. These maps provide the basis for the direct quantification of length, width and area of interpreted architectural elements in the ESB.

4. Seismic-stratigraphic units and associated architectural elements

4.1 Unit 1

The lowermost Unit 1 (Upper Cretaceous to Paleocene) is bounded at its top by horizon H1, a mid-Eocene unconformity with regional expression (Baudon and Cartwright, 2008; Fiduk et al., 2004) (Fig. 3). Unit 1 shows continuous reflections of low to moderate amplitude, (Fig. 3). However, high-amplitude reflections occur within a Paleocene Canyon (C0) and in horizon Pal-1 (Fig. 3).

4.1.1 Sand-prone strata

Two types of sand-prone elements are observed in Unit 1. Canyon C0 forms the main sand-prone feature in Unit 1 (Fig. 3 and 3), reaching a maximum width of 3000 m and a thalweg height of 228 m. Maximum amplitude maps show regions of high amplitude in C0, with lengths of 1 to 2 km (Fig. 4a). These features are interpreted as sand-prone strata, being larger in volume (and closer together) towards the distal part of Canyon C0 (Fig. 4a). Discontinuous channel-fill deposits in C0 show lower continuity and smaller dimensions towards the upper continental slope (Fig. 4a).

A secondary sand-prone interval is interpreted in the vicinity of horizon Pal-1, in Unit 1 (Fig. 3 and 4c). On vertical seismic sections, Pal-1 is intersected by numerous faults (Fig. 3 and 4c). RMS amplitude maps centred in horizon Pal-1 show the highest amplitudes close to salt ridges and in the salt-withdrawal basin, where Pal-1 intersects the flanks and base of Canyon C0 (Fig. 4c).

4.1.2 Crestal, radial and synclinal faults

Unit 1 is cut by crestal and synclinal faults *sensu* Alves et al (2009) (Figs. 3, 4b and 4c). These faults propagate throughout the vertical extent of Unit 1 and are truncated by horizon H1 (Fig. 3). A limited number of faults show reactivation and vertical propagation into Unit 2 (Baudon and Cartwright, 2008; Omosanya and Alves, 2014). Coherence and RMS amplitude maps suggest a close relationship between the strikes of crestal faults and underlying salt structures (Figs. 4b and 4c). In the western sector of the basin, crestal faults strike NW-SE and are intersected by E-W striking faults (Fig. 4d). Towards the East, crestal fault meshes follow a predominant NE-SW strike with a conjugate NW-SE fault family (Fig. 4e). These faults often link to radial faults in the proximity of diapirs but the distinction between both types is not always clear (Fig. 4c).

Synclinal faults occur predominantly within the main salt withdrawal basin, and bound Canyon C0 (Figs. 3, 4b and 4c). The faults strike N-S and are associated with conjugate faults that follow a

range of strikes between N45 and N120 (Fig. 4f). Synclinal and crestal/radial faults show a degree of dimensional clustering between them (Fig. 5). Synclinal faults are larger, between 2200 m and 4700 m, whereas crestal/radial faults show lengths between 860 m and 2500 m. Fault throws of both families have minimum values of 50 m. However, crestal faults have higher throws, up to 204 m compared to the 124 m observed for synclinal faults (Fig. 5a). Clustering is also observed between fault length and spacing (Fig. 5b). Synclinal faults are spaced between 192 m and 155 m, whereas crestal faults are spaced between 204 m and 680 m (Fig. 5b).

RMS and maximum amplitude maps within Unit 1 show numerous faults in the main salt-withdrawal basin and near salt diapirs (Fig. 4c). These faults delimit multiple (seismic-scale) compartments whose dimensions can be extrapolated from the measured fault data. As a result, fault length and fault spacing are associated to the length and width of the compartments (blocks) they bound. In the study area, crestal faults are prone to create a larger number of smaller fault-bounded blocks in Unit 1 when compared to strata crossed by synclinal faults (Figs. 4 and 5).

4.2 Unit 2

Unit 2 is delimited by the middle Eocene unconformity (horizon H1) at its base and by horizon H2 at its top (Fig. 3). Strata in Unit 2 is of moderate to high amplitude. According to Fiduk et al. (2004), high-amplitude features are generated by reflective volcaniclastic material in Unit 2, most of it sourced from the Abrolhos Bank. The main architectural elements occurring in the Unit are laterally continuous mass-transport deposits (MTDs) and turbidite lobes (Fig. 3, 6 and 7).

4.2.1 Mass-Transport Deposits (MTDs)

Five major MTDs occur in Unit 2. They show variable amplitude and chaotic to semi-transparent seismic reflections (Fig. 3 and 6). Eocene-Oligocene MTDs comprise over 60% of Unit 2 around

the western diapir ridge, and up to 67.7% within the main salt-withdrawal basin. These values drop to a minimum of 38% in the vicinity of the eastern salt ridge (see Supplementary Material, Fig. S1). Identical trends are observed for average thickness, which decreases eastwards from 80 m to ~ 50 m.

The lowermost mass-transport deposit (MTD-A1) in Unit 2 contains multiple blocks (Fig. 6a and 6c). Mass-transport blocks are often linked to underlying faults showing identical strikes to their flanks (Figs. 6a and 6b). The occurrence of blocks in clusters above crestal faults suggests a genetic link between MTD-A1, overburden faulting and salt growth (Gamboa et al., 2011; Gamboa et al., 2012a).

RMS amplitudes are variable in MTD-A2, particularly towards the main salt-withdrawal basin (Fig. 6d). The high-amplitude strata observed in the eastern part of MTD-A2 may reflect the presence of deformed blocks without well-defined flanks (Fig. 6d). Other MTDs in Unit 2 tend to have identical seismic facies to MTD-A2, with chaotic or low-amplitude internal reflections (Fig. 3). Overall, MTDs show decreasing tendency in their width and thickness towards the top of Unit 2 (Fig. 3, see also supplementary material Fig. S1).

4.2.2 Turbidite lobes

Turbidites show uniform, high-amplitude reflections, and variable lateral continuity. They separate, or are interbedded, with recurrent MTDs (Fig. 3 and 7). Twenty reflections were mapped in a central area of recurrent mass-wasting, from which nine are represented in Figure 7a. Turbidite lobes are identified in the lower half of Unit 2 (Fig. 7a and 7b). These turbidites tend to have higher vertical offsets due to the presence of thick MTDs between them. Such a trend is reversed towards the upper part of Unit 2, as seismic reflections have a marked lateral continuity and vertical proximity (Figs. 3 and 7a).

High-amplitude zones within the turbidite lobes follow a NW-SE strike, parallel to their long axes (Figs. 7a, 7b and 7c). Amplitude decreases laterally towards the edges of the lobes, as observed in S2 (Fig. 7c), or show downslope variations, as in S3 (Fig. 7d). Amplitude variations suggest that intra-lobe features were perched against salt diapirs, in essence recording interactions between intra-lobe channels and salt-related topography. These thin channelised features are also prone to have coarser, homogenous sediments, compartmentalising the lobes at smaller scales of observation. In contrast, linear low-amplitude features can represent channelised features filled with mud-prone or heterogeneous sediment, i.e. forming lateral permeability baffles.

4.3 Unit 3

The base of Unit 3 is inferred to be early Miocene in age, and is bounded at its top by the seafloor. Unit 3 can be divided into three sub-units (Fig. 8). The lowermost sub-unit 3a represents an Early Miocene canyon system (Canyon C1). This canyon is overlain by sub-units 3b and 3c, which show multiple erosional features. Several MTDs occur in sub-unit 3c. The youngest feature in Unit 3 is the modern Rio Doce canyon, named Canyon C2 in this paper (Fig. 1b and 8).

4.3.1. Axial canyons

The two submarine canyons observed in the salt-withdrawal basin have similar geometry, with upslope tributaries merging at specific confluence points (Fig. 8b and 8c). Canyon C1 is filled by high-amplitude strata (Figs. 3a and 8). Confluence points occur in areas of topographic confinement imposed by diapirs (Fig. 1b) (Gamboa et al., 2012b). The tributaries and post-confluence segment of this canyon have straight morphologies, and the junction of these segments does not show a significant offset (Fig. 8b). The height of Canyon C1 reaches a maximum of 150 m upslope, increasing to 250 m downslope. Its width ranges between 1000 to 1700 m on the upper slope,

increasing sharply to values between 2500 m and 3000 m at the confluence point (see Supplementary Material, Fig. S2).

Canyon C2 presents a distinct geometry when compared to C1 (Fig. 8c), with its confluence point located between diapirs D2 and D6 (Fig. 1b). Its tributaries are relatively straight and merge at an unequal confluence (Gamboa et al., 2012b). These same tributaries show distinct dimensional trends (see Supplementary Material, Fig. S3), whereas highly sinuous thalwegs are observed in the post-confluence sector (Fig. 1b and 8c). Maximum thalweg heights on the western and eastern tributaries reach 140 m and 180 m, respectively, but both values decrease towards the confluence. In post-confluence areas, thalweg width increases to 200 m. The width of the tributaries and post-confluence channel range between 350 m and 700 m. An exception to these values is observed at the confluence point, where thalweg width abruptly increases to 1270 m (see Supplementary Material, Fig. S3).

4.3.2. Slope channel systems

Channel density maps show that a larger number of channels occurs along two elongated areas merging within the region of diapir confinement (see Area 1 in Fig. 9). In parallel, channel density decreases towards the lower slope. A marked transition between the two areas is recorded at the channel confluences (Areas 2 and 3; Fig. 9).

Sub-unit 3b comprises a Miocene channel system showing U- and V-shaped incision surfaces, and smaller gullies, along the topographically confined slope (Fig. 8a). Incision surfaces have average widths of 660 m, for a range between 86 m and 2500 m. Average height reaches 58 m, ranging from 10 m to 167 m (see Supplementary Material, Fig. S4). The interpreted data show a downslope increase in the width of the channels, away from the regions of greater topographic confinement (Gamboa et al., 2012b). Circular to elliptical depressions are observed on the northeast

limit of the slope (Heiniö and Davies, 2009) (Fig. 9b). In addition, larger depressions have been observed in mid-slope locations (Fig. 9b). Despite their apparent alignment, the bowl-shaped geometry of these erosional features is likely to limit the connectivity between depressions and their infilling strata.

Sub-unit 3c corresponds to the uppermost stratigraphic package in the ESB, comprising Pliocene to Holocene strata. Its architecture contrasts with sub-unit 3b due to the occurrence of continuous high-amplitude and chaotic reflections in MTDs (Fig. 8a). MTDs are more abundant at the base of sub-unit 3c, decreasing in thickness towards its top. Such a stratigraphic architecture, and associated seismic character, share some affinity with Unit 2. However, the degree of topographic confinement imposed by diapirs is higher in sub-unit 3c, and multiple submarine channels are observed in the study area at this level. Variations in the trends of plotted curves indicate a downslope decrease in thalweg height and an increase in the width of these younger channels (see Supplementary Material, Fig. S4).

5. Scale relationships of seismic-scale architectural elements

In this section we show comparative scale-relationships for interpreted architectural elements. In our measurements we considered architectural elements to be seismic-scale features with a characteristic geometry and seismic facies. Quantitative analyses focused on 3rd order elements or loop sets, as defined by Prather (2000), and are comparable to the fundamental architectural units defined by McHargue (2011).

Given that important limitations arise when determining best fits to the different data series, a simplified method was used to compare the range of scales observed in the ESB (Fig. 10). This consisted on the fitting of origin-intersecting linear trends to all data series, thus allowing the width

(W) to be represented as a direct proportion of height (H). Thus, width-height scale relationships are defined mathematically as:

$$W = \alpha \cdot H \qquad \text{(eq. 1)}$$

where α is a constant of proportionality equal to the slope of the regression line. Similarly, the relations between length (L) and width (W) of architectural elements is represented as:

$$L = \beta \cdot W \qquad \text{(eq. 2)}$$

Distinct lines with variable slope values of α or β were used to estimate the maximum (α_{MAX}, or β_{MAX}) and minimum (α_{MIN}, or β_{MIN}) scale relationships, or ratios, for each data series and thus complement the information provided by the best fit lines (Table 1). Log-log plots were used to represent the data, and resuting scale-relationships were compiled in Figures 10 and 12, and Table 1.

5.1. Mass-Transport Deposits

MTDs comprise the largest architectural elements in the study area. They are characterised by average ratios of W/H >100, and can be sub-divided in two clusters. The larger MTDs are observed in Unit 2, and show an average W/H ratio (α) of 249 - for minimum and maximum values of 150 and 350. Such a range of values reflects a tendency for MTDs to decrease in size towards the top of Unit 2. The largest W/H ratios (~350) correspond to MTDs that are up to 30000 m in width, and are located in the lower part of Unit 2 (MTDA-1, MTD-A2 and MTD-A3). Contrastingly, MTDs in the

upper part of Unit 2 have widths as low as 12000 m, less than half the width of the deeper MTDs (Fig. 10a).

The largest MTDs in Unit 3 are narrower than 9500 m. These are values observed at the top of Unit 2. Scale relationships of 197.3 were obtained for MTDs in Unit 3, varying between 150 and 290 (Table 1). MTDs in Unit 2 are twice to 10 times larger than in Unit 3, but the W/H ratios of MTDs in these two units show ranges that only differ by ~30% (Fig. 10a).

5.2. Mass-transport blocks

Mass-transport blocks are limited to MTD-A1 in the study area (Fig. 3 and 6). Crestal faults deform the strata underlying MTD-A1 and influence the shape and size of mass-transport blocks, particularly when both features occur in similar areas of the continental slope, have identical strikes (Fig. 6b) and present vertical continuity (Fig. 6a) (Gamboa et al., 2011). The width of mass-transport blocks varies between 105 m and 1500 m, and their length between 235 m and 2420 m. Block height ranges from 47 m to 250 m (Fig. 10a), values that are similar to the thickness of the MTD in which they are observed. Scale relationships show W/H ratios of 3 for the MTD blocks, ranging between 1 and 10 (Table 1). Length and width (L/W) relationships of failed blocks show best-fit β ratios of 1.6, with maximum and minimum values of 1 and 5, respectively (Fig 10b, Table 1).

5.3. Turbidite lobes

Individual turbidite lobes have an average width between 1600 m and 8500 m, and height between 23 m and 50 m (Fig. 10a). Turbidite lobes show W/H ratios of 99.7, ranging between 40 and 310 (Table 1). However, this clustering of values suggests W/H ratios between 60 and 100 to be more representative (Fig. 10a). Length-width (L/W) relationships are also significantly variable

(Fig. 10b). The average width of turbidite lobes ranges between 1620 m and 8500 m, for lengths varying between 4645 m and 29970 m. The trends obtained show L/W ratios of 2.9 for turbidite lobes, ranging between 1 and 7 (Table 1).

5.4. Submarine channels and canyons

The larger channelled features in the ESB are submarine canyons in Unit 1 (Canyon C0) and Unit 3 (Canyons C1 and C2) incising the salt-withdrawal basin (Fig. 3 and 8a). Buried canyons C0 and C1 show a similar W/H ratio of 12, and identical minimum and maximum ratios (Figures 10a and 11, and Table 1). Canyon C2 shows a smaller W/H ratio of 4, varying between 2 and 14 (Figures 10a and 11, and Table 1). W/H values for C2 are about 3 to 3.5 times smaller than the ratios obtained for buried canyons.

The multiple channels identified in sub-units 3b and 3c have smaller sizes, but a much broader dimensional range, than their buried counterparts. Linear regression lines for features in sub-unit 3b show W/H ratios of 11, ranging between 3 and 80 (Table 1). Similar W/H ratios were estimated for sub-unit 3c, with fitted ratios of 13.7. However, W/H ratios are highly variable - ranging between 4 and 120 (Table 1).

Width/Height scale relationships for Cenozoic channels and canyons are better assessed using average values (Fig. 11). Thus, canyons can be compared using the average width and height of each tributary and post-confluence segment (Fig. 8). Channel systems in sub-units 3b and 3c were separated in three distinct areas, A1 to A3, each with variable topographic confinement (Fig. 9a). The results in Figure 11 show buried axial canyons to have average width and heights 2 to 3 times larger than younger channels in sub-units 3b and 3c. Buried submarine canyons show identical W/H scale relationships, with average values showing a ratio of approximately 12 (Fig. 11). This

relationship is maintained between tributaries and the post-confluence segment in Canyon C1, despite a downslope increase in width and height (Fig. 11).

Similarities in scale between canyon segments are not observed in Canyon C2. The unequal character of its confluence is reflected in the scale relationships obtained, with the eastern tributary and post-confluence segment showing a W/H ratio close to 4, whereas the western tributary shows a ratio of 6.5 (Fig. 11). In comparison, channels in sub-units 3b and 3c show a wider range of average width and height scale relationships, with ratios between 10 and 18 (Fig. 10a and 11).

5.5. Faults and fault-bounded blocks

The dimension of fault-bounded blocks is inherently controlled by the length and spacing of their bounding faults. When comparing the two fault families in Unit 1 a key observation in this work is that, for identical spacing values, the length of synclinal faults is about twice of that recorded by crestal faults (Fig. 5). This character results in divergent L/W scaling relationships between the two types of fault-bounded blocks interpreted. Average L/W ratios for blocks delimited by synclinal faults approach a value of 9.7 (ranging between 7.3 and 17.5), whereas the L/W ratio for blocks delimited by crestal faults is ~3, with a maximum L/W ratio of 5.5 (Fig. 10b, Table 1). As a result, synclinal faults tend to delimit fault-bound blocks that are 3 to 4 times longer than those delimited by crestal faults (Fig. 10b).

6. Discussion

6.1. Distribution of compartmentalised sand-prone strata in the ESB

Reservoir units in deep-offshore settings consist of heterogeneous sandy turbidites deposited as submarine channels and fans (Clark and Pickering, 1996; Mayall et al., 2006; Moraes et al., 2006;

Prather, 2003). Submarine channels and lobes identified in the ESB comprise reservoir-prone elements similar to proven exploration targets in SE Brazil. For instance, Canyon C0 is comparable to the Golfinho Field and Regência discoveries in the ESB (Bruhn and Walker, 1997; Fiduk et al., 2004; Vieira et al., 2007; Vincentelli et al., 2007). Discoveries in Eocene and Oligocene strata of the ESB - exemplified by the Cangoá field (Vincentelli et al., 2007) - and turbidite reservoirs in the Campos basin (De Gasperi and Catuneanu, 2014), are identical to the turbidite lobes in Unit 2. These lobes show thickness values similar to producing deepwater reservoirs, in the order of 20 to 30 m (Hardage et al., 1998; Prather et al., 2000; Puckette and Al-Shaieb, 2003).

In the ESB, reservoir-prone elements reveal changing architectures through time as a function of the interaction between salt-controlled topography, the emplacement of the volcanic Abrolhos Bank, and external factors influencing sediment supply to the basin (Fiduk et al., 2004; Gamboa et al., 2010; Mohriak, 2003; Mohriak, 2005; Mohriak et al., 2012). The most important combination of tectonic and depositional events occurred during the mid-Eocene-Oligocene times in the ESB, when intense volcanic activity, tectonic uplift and associated sediment input resulted in widespread halokinesis (Ferreira et al., 2014; Mohriak et al., 2012). These events altered basin morphology, forcing a shift in the strike of the continental slope from N-S to E-W in the northern part of the ESB (Fig. 1). Consequently, gravity flows gradually acquired a NW-SE to N-S strike, sub-parallel to the strike of the interpreted salt ridges (Fig. 1, see also Schreiner et al. (2009)). This latter setting contrasts with the generalised E-W strike of turbidite systems in the southern ESB, Campos and Santos basins, which tend to flow perpendicularly to elongated salt structures and regional structural trends (De Gasperi and Catuneanu, 2014; Fetter, 2009; Viana et al., 1998).

Axial canyons are the main sand-prone architectural elements in the ESB (Fig. 3, 4 and 8). Slope compartmentalisation induced by canyons will depend primarily from changes in their geometry and sizes. In the examples given in this paper, canyon tributaries can constitute relevant upslope compartments for sand, in addition to the larger downslope (i.e. post-confluence) segments. The

main exploration risk in submarine canyons is the heterogeneity of their sedimentary fill (Link and Weimer, 1991). Thus, RMS amplitude data in this paper suggest that sand-prone strata predominantly occur towards downslope domains in the ESB (Fig. 4a), with lateral compartmentalisation in submarine canyons being influenced by the continuity of channel-fill deposits and lateral accretion packages in meandering segments (Abreu et al., 2003; Deptuck et al., 2007; Mayall et al., 2006).

The scattered channels observed in Units 3b and 3c reveal major uncertainties in their locations and geometry (Figs. 3 and 8). These relatively young channels are prone to form multiple sand-bodies with limited lateral contact. Nevertheless, slope regions where higher channel densities occur may have channels in closer proximity due to their shorter lateral spacing and vertical stacking (Fig. 9a). This latter character can improve the vertical connectivity between different channels, especially when young thalwegs incise into the sand-rich levels of older submarine channels (McKie et al., 2010; Snedden, 2013).

Salt structures play an important control on the distribution of channels in Unit 3. The increasing slope confinement imposed by diapirs D2 and D6 forced the channel systems to coalesce, decreasing the lateral scatter of channels towards the lower slope - thus limiting uncertainty in their locations (Fig. 9). As a result, channels in lower slope areas occur close to the axis of the salt-withdrawal basin. Secondary channels are observed along the flanks of the diapirs, where morphological depressions also occur, but these depressions constitute semi-isolated (stratigraphic) compartments with limited lateral connectivity (Fig. 9b). They are more frequent to the west of the study area (Fig. 9b).

Turbidite lobes in Unit 2 are wider and have lower heights than submarine channels as a result of lower lateral confinement during deposition (Fig. 10). The size of these turbidite lobes is mainly controlled by the occurrence of thick, low permeability MTDs and associated salt diapirs (Fig. 7). MTD deposition is not only interpreted to decrease the size of turbidite lobes but can also result in

vertical offsets of 100's of metres between turbidite sands (Fig. 10). The distribution and dimensions of MTDs can therefore be used as a proxy to assess the degree of connectivity between intercalated sand-bodies; turbidites occurring in the vicinity of the western diapir ridge are associated with higher exploration risks due to their relative smaller sizes and the occurrence of MTDs (Fig. 6, Supplementary Material S1).

The distribution of crestal and synclinal faults at deeper stratigraphic levels controls the location, size and number of blocks bounded by each fault family (Figs. 3, 4b and 5). Blocks bounded by crestal faults occur in high number and show relatively small sizes near the diapir ridges, often intersecting sand-prone, high-amplitude areas (Figs. 3, 4 and 10b). In contrast, faulted blocks delimited by synclinal faults in the salt-withdrawal basin are larger and in lower number, intersecting high-amplitude overbank strata of Canyon C0 (Fig. 4). These contrasting characters suggest higher connectivity close to the salt ridges, where crestal faults predominate. In contrast, large blocks bounded by synclinal faults correlate with lower risks and lower fault compartmentalisation. However, these areas show an increased degree of uncertainty due to the nature (and distribution) of coarse-grained sediment on the overbanks of Canyon C0 (Fig. 4).

6.2. Comparative scale-relationships of architectural elements

The aspect ratios calculated for different architectural elements highlight important dimensional overlaps (Fig. 12). Such overlaps are particularly relevant between elements showing closer genetic processes, e.g. the W/H ratios of channels and depressions created by erosive flows, or poorly confined turbidite and associated MTDs (Fig. 12a). The L/W ratios of architectural elements show a limited range between 1 and 17.5 (Fig. 10b). Turbidite lobes stand out as the elements with the larger dimensional cluster and L/W ratio dispersion, whereas the remaining elements show similar sizes and dimensional overlaps (Fig. 12b). These similarities in sizes and dimensions derive from their common genesis, as in the case of MTD blocks and crestal faults (Fig. 6a) (Gamboa et al.

2011). However, identical sizes and aspects ratios are also observed between elements with no genetic affinity, such as mass-transport blocks, erosive channels and depressions (Fig. 10 and 12).

A striking result from this work is that identical aspect ratios are maintained between common elements in distinct units. Such a character is observed, for instance, in Canyons C0 and C1. Despite the significant time gap between the two, both canyons show W/H ratios of 12 (Fig. 11). Similar ratios are also observed for channels in sub-unit 3c. The MTDs in Units 2 and 3 also share identical aspect ratios, between 150 and 300, despite their different sizes (Fig. 10a). In addition, these MTDs have also been emplaced within increasingly confined depocentres, while maintaining a upward invariability in their scale-relationships.

Based on these results, we suggest that the topographic confinement imposed by salt structures exerts a key control on the aspect ratio of the interpreted architectural elements. This control results in common aspect ratios, for similar architectural elements, in time and space.

7. Conclusions

This work focuses identified and quantified the geometry of deepwater architectural elements in three distinct Cenozoic stratigraphic units of the ESB. Our results show that:

- The distribution and dimensions of architectural elements are controlled by salt-related faults and associated seafloor topography. The higher dimensional variability, and lower continuity, of sand-prone elements at the vicinity of diapir ridges demonstrates an important degree of structural and stratigraphic compartmentalisation in these areas.
- Stratigraphic compartmentalisation tends to predominate towards the axis of salt-withdrawal basins, controlled by depositional heterogeneities in channels and turbidite lobes.
- Erosion plays a key role in strata connectivity, leading to important dimensional variability in permeable units. Turbidite lobes show important lateral and vertical variability related to subsequent erosion by MTDs. In submarine channel systems, erosion can increase the

vertical connectivity in regions where vertical stacking, and higher channel density, are observed.

- Dimensional overlaps and identical scale relationships are observed for distinct architectural elements in the ESB. Importantly, scale relationships were maintained through space and time for common architectural elements deposited under increasing topographic confinement.

The approach in this paper is relevant for hydrocarbon exploration on continental margins by assessing the relative continuity of sand-prone architectural elements on salt-rich continental slopes. As a corollary, we show that structural and depositional compartmentalisation are chiefly controlled by basin geometry.

Acknowledgements

The authors thank CGG for the permission to publish the data presented in this paper. Schlumberger is acknowledged for the provision of seismic interpretation software. D. Gamboa thanks the Fundação para a Ciência e a Tecnologia (FCT) for the SFRH/BD/38819/2007 PhD grant. We would like to thank B. Bosworth for editorial support, and W. Mohriak and an anonymous reviewer for their constructive comments.

References

Abreu, V., Sullivan, M., Pirmez, C. and Mohrig, D., 2003. Lateral accretion packages (LAPs): an important reservoir element in deep water sinuous channels. Marine and Petroleum Geology, 20(6-8): 631-648.

Ainsworth, R.B., 2010. Prediction of stratigraphic compartmentalization in marginal marine reservoirs. In: S.J. Jolley, Q.J. Fisher, R.B. Ainsworth, P. Vrolijk and S. Delisle (Editors), Reservoir Comparmentalization. Geological Society Special Publication, Vol 347, pp. 199-218.

Alves, T.M., 2010. 3D Seismic examples of differential compaction in mass-transport deposits and their effect on post-failure strata. Marine Geology, 271(3-4): 212-224.

Alves, T.M., 2012. Scale-relationships and geometry of normal faults reactivated during gravitational gliding of Albian rafts (Espírito Santo Basin, SE Brazil). Earth and Planetary Science Letters, 331–332(0): 80-96.

Alves, T.M., Cartwright, J. and Davies, R.J., 2009. Faulting of salt-withdrawal basins during early halokinesis: Effects on the Paleogene Rio Doce Canyon system (Espírito Santo Basin, Brazil). AAPG Bulletin, 93(5): 617-652.

Barker, P.F., Buffler, R.T. and Gambôa, L.A., 1983. A seismic reflection study of the Rio Grande Rise. In: P.F. Barker, R.L. Carlson and D.A. Hohnson (Editors), Initial Reports of the Deep Sea Drilling Program, Washington, D.C., Government Printing Office, pp. 953-976.

Baudon, C. and Cartwright, J., 2008. The kinematics of reactivation of normal faults using high resolution throw mapping. Journal of Structural Geology, 30(8): 1072-1084.

Bruhn, C.H.L. and Walker, R.G., 1997. Internal architecture and sedimentary evolution of coarse-grained, turbidite channel-levee complexes, early eocene Regência canyon, Espirito Santo Basin, Brazil. Sedimentology, 44(1): 17-46.

Clark, I.R. and Cartwright, J.A., 2009. Interactions between submarine channel systems and deformation in deepwater fold belts: Examples from the Levant Basin, Eastern Mediterranean sea. Marine and Petroleum Geology, 26(8): 1465-1482.

Clark, J.D. and Pickering, K.T., 1996. Architectural elements and growth patterns of submarine channels; application to hydrocarbon exploration. AAPG Bulletin, 80(2): 194-221.

Cobbold, P.R., Meisling, K.E. and Mount, V.S., 2001. Reactivation of an obliquely rifted margin, Campos and Santos basins, southeastern Brazil. AAPG Bulletin, 85(11): 1925-1944.

Davison, I., 1999. Tectonics and hydrocarbon distribution along the Brazilian South Atlantic margin. In: N.R. Cameron, R.H. Bate and V.S. Clure (Editors), The oild and gas habitats of the South Atlantic. Geological Society London Special Publications 153, pp. 133-151.

De Gasperi, A. and Catuneanu, O., 2014. Sequence stratigraphy of the Eocene turbidite reservoirs in Albacora field, Campos Basin, offshore Brazil. AAPG Bulletin, 98(2): 279-313.

Demercian, S., Szatmari, P. and Cobbold, P.R., 1993. Style and pattern of salt diapirs due to thin-skinned gravitational gliding, Campos and Santos basins, offshore Brazil. Tectonophysics, 228(3-4): 393-433.

Deptuck, M.E., Sylvester, Z., Pirmez, C. and O'Byrne, C., 2007. Migration-aggradation history and 3-D seismic geomorphology of submarine channels in the Pleistocene Benin-major Canyon, western Niger Delta slope. Marine and Petroleum Geology, 24(6-9): 406-433.

Fainstein, R. and Summerhayes, C.P., 1982. Structure and origin of marginal banks off Eastern Brazil. Marine Geology, 46(3-4): 199-215.

Ferreira, T.S., Araújo, M.N.C.d. and Alves da Silva, F.C., 2014. Cenozoic folding in the Cumuruxatiba basin, Brazil: An approach to the deformation trigger by the Abrolhos magmatism. Marine and Petroleum Geology, 54(0): 47-64.

Fetter, M., 2009. The role of basement tectonic reactivation on the structural evolution of Campos Basin, offshore Brazil: Evidence from 3D seismic analysis and section restoration. Marine and Petroleum Geology, 26(6): 873-886.

Fiduk, J.C., Brush, E.R., Anderson, L.E., Gibbs, P.B. and Rowan, M.G., 2004. Salt deformation, magmatism, and hydrocarbon prospectivity in the Espirito Santo Basin, offshore Brazil. In: P.J. Post et al. (Editors), Salt-sediment interactions and hydrocarbon prospectivity: Concepts, applications, and case studies for the 21st century. GCSSEPM 24th Annual Research Conference, pp. 370-392.

França, R.L., Del Rey, A.C., Tagliari, C.V., Brandão, J.R. and Fontanelli, P.R., 2007. Bacia de Espírito Santo. Boletim de Geociências da Petrobras, 15(2): 501-509.

Gamboa, D., Alves, T. and Cartwright, J., 2011. Distribution and characterization of failed (mega) blocks along salt ridges, southeast Brazil: Implications for vertical fluid flow on continental margins. Journal of Geophysical Research, 116(B8): B08103.

Gamboa, D., Alves, T., Cartwright, J. and Terrinha, P., 2010. MTD distribution on a 'passive' continental margin: The Espírito Santo Basin (SE Brazil) during the Palaeogene. Marine and Petroleum Geology, 27(7): 1311-1324.

Gamboa, D., Alves, T.M. and Cartwright, J., 2012a. Seismic-Scale Rafted and Remnant Blocks over Salt Ridges in the Espírito Santo Basin, Brazil. In: Y. Yamada et al. (Editors), Submarine Mass Movements and Their Consequences. Springer, pp. 629-638.

Gamboa, D., Alves, T.M. and Cartwright, J., 2012b. A submarine channel confluence classification for topographically confined slopes. Marine and Petroleum Geology, 35(1): 176-189.

Hardage, B.A., Simmons, J.J.L., Pendleton, V.M., Stubbs, B.A. and Uszynski, B.J., 1998. 3-D seismic imaging and interpretation of Brushy Canyon slope and basin thin-bed reservoirs, northwest Delaware Basin. Geophysics, 63(5): 1507-1519.

Heiniö, P. and Davies, R.J., 2009. Trails of depressions and sediment waves along submarine channels on the continental margin of Espirito Santo Basin, Brazil. Geological Society of America Bulletin, 121(5-6): 698-711.

Lasseter, T.J., Waggoner, J.R. and Lake, L.W., 1986. Reservoir heterogeneities and their influence on ultimate recovery. In: L.W. Lake and H.B. Carroll (Editors), Reservoir Characterisation. Academic Press, Orlando, pp. 545-559.

Link, M. and Weimer, P., 1991. Seismic facies and sedimentary processes of submarine fans and turbidite systems: An overview. In: P. Weimer and M. Link (Editors), Seismic facies and sedimentary processes of submarine fans and turbidite systems. Springer, pp. 3-7.

Love, F. et al., 2005. Northern Espírito Santo basin canyon models ancient sand transport. Offshore, March 2005: 74-78.

Mayall, M., Jones, E. and Casey, M., 2006. Turbidite channel reservoirs--Key elements in facies prediction and effective development. Marine and Petroleum Geology, 23(8): 821-841.

Mayall, M. et al., 2010. The response of turbidite slope channels to growth-induced seabed topography. AAPG Bulletin, 94(7): 1011-1030.

McHargue, T. et al., 2011. Architecture of turbidite channel systems on the continental slope: Patterns and predictions. Marine and Petroleum Geology, 28(3): 728-743.

McKie, T., Jolley, S.J. and Kristensen, M.B., 2010. Stratigraphic and structural compartmentalization of dryland fluvial reservoirs: Triassic Heron Cluster, Central North Sea. In: S.J. Jolley, Q.J. Fisher, R.B. Ainsworth, P. Vrolijk and S. Delisle (Editors), Reservoir Compartmentalization. Geological Society Special Publication, Vol 347, pp. 165-198.

Mohriak, W.U., 2003. Bacias sedimentares da margem continental Brasileira. In: L.A. Bizzi, C. Schobbenhaus, R.M. Vidotti and J.H. Goncalves (Editors), Geologia, Tectonica e Recursos Minerais do Brasil. CPRM, Brasilia, pp. 87-165.

Mohriak, W.U., 2005. Interpretação geológica e geofísica da Bacia do Espírito Santo e da região de Abrolhos: Petrografia, datação radiométrica e visualização sísmica das rochas vulcânicas. Boletim de Geociencias da Petrobras, 14(1): 133-142.

Mohriak, W.U., Nemcok, M. and Enciso, G., 2008. South Atlantic divergen margin evolution: rift-borded uplift and salt tectonics in the basins of Southeastern Brazil. In: R.J. Pankhurst, R.A.J. Trouw, B.B. Brito Neves and M.J. de Wit (Editors), West Gondwana pre-Cenozoic correlations across the South Atlantic region. Geological Society London, Special Publications 294, pp. 365-398.

Mohriak, W.U., Rabelo, J.H.L., De Matos, R.D. and De Barros, M.C., 1995. Deep seismic reflection profiling of sedimentary basins offshore Brazil: geological objectives and preliminary results in the Sergipe Basin. Journal of Geodynamics, 20(4): 515-539.

Mohriak, W.U., Szatmari, P. and Anjos, S., 2012. Salt: geology and tectonics of selected Brazilian basins in their global context. In: G.I. Alsop, S.G. Archer, A.J. Hartley, N.T. Grant and R. Hodgkinson (Editors), Salt Tectonics, Sediments and Prospectivity. Geological Society, London, Special Publications 363, pp. 131-158.

Moraes, M.A.S., Blaskovski, P.R. and Paraizo, P.L.B., 2006. Arquitectura de reservatorios de aguas profundas. Boletim de Geociencias da Petrobras, 14(1): 7-25.

Mutti, E. and Normark, W.R., 1991. An integrated approach to the study of turbidite systems. In: P. Weimer and M. Link (Editors), Seismic Facies and Sedimentary Processes of Submarne Fans and Turbidite Systems. Springer, pp. 75-106.

Ojeda, H.A.O., 1982. Structural framework, stratigraphy, and evolution of Brazilian marginal basins. AAPG Bulletin, 66(6): 732-749.

Omosanya, K.d.O. and Alves, T.M., 2014. Mass-transport deposits controlling fault propagation, reactivation and structural decoupling on continental margins (Espírito Santo Basin, SE Brazil). Tectonophysics, 628(0): 158-171.

Omosanya, K.O. and Alves, T.M., 2013. A 3-dimensional seismic method to assess the provenance of Mass-Transport Deposits (MTDs) on salt-rich continental slopes (Espírito Santo Basin, SE Brazil). Marine and Petroleum Geology, 44: 223-239.

Pilcher, R.S., Kilsdonk, B. and Trude, J., 2011. Primary basins and their boundaries in the deep-water northern Gulf of Mexico: Origin, trap types, and petroleum system implications. AAPG bulletin, 95(2): 219-240.

Prather, B.E., 2003. Controls on reservoir distribution, architecture and stratigraphic trapping in slope settings. Marine and Petroleum Geology, 20(6-8): 529-545.

Prather, B.E., Keller, F.B. and Chapin, M.A., 2000. Hierachy of deep-water architectural elements with reference to seismic resolution: implications for reservoir prediction and modeling. In: P. Weimer et al. (Editors), Deepwater Reservoirs of the World, GCSSEPM Foundation 20th Annual Research Conference, pp. 817-834.

Puckette, J. and Al-Shaieb, Z., 2003. Naturally underpressured reservoirs: applying the compartment concept to the safe disposal of liquid waste. Search and Discovery article, 40071.

Pyles, D.R., 2007. Architectural Elements in a Ponded Submarine Fan, Ross Sandstone, Ireland. In: T.H. Nilsen, R.D. Shew, G.S. Steffens and J.R. Studlick (Editors), Atlas of Deepwater Outcrops, AAPG Studies in Geology 56. Shell Exploration and Production and American Association of Petroleum Geologists, pp. 206-209.

Schreiner, S., de Souza, M.B.F.M. and Migliorelli, J.P.R., 2009. Modelo digital da geomorfologia do fundo oceânico do centro-sul da Bacia do Espírito Santo e norte da Bacia de Campos. Boletim de Geociencias da Petrobras, 17(2): 365-369.

Slatt, R.M. (Editor), 2006. Stratigraphic Reservoir Characterization for Petroleum Geologists, Geophysicists and Engineers. Handbook of Petroleum Exploration and Production, Volume 6, Volume 6. Elsevier, 478 pp.

Slatt, R.M., Eslinger, E.V. and Van Dyke, S.K., 2009. Acoustic and petrophysical properties of a clastic deepwater depositional system from lithofacies to architectural elements' scales. Geophysics, 74(2): WA35-WA50.

Smith, R., 2004. Silled sub-basins to connected tortuous corridors: Sediment distribution systems on topographically complex sub-aqueous slopes. In: S.A. Lomas and P. Joseph (Editors), Confined Turbidite Systems. Geological Society of London, Special Publication, 222, pp. 23-43.

Snedden, J.W., 2013. Channel-body basal scours: Observations from 3D seismic and importance for subsurface reservoir connectivity. Marine and Petroleum Geology, 39(1): 150-163.

Sobreira, J.F.F. and França, R.L., 2005. A tectono-magmatic model for the Abrolhos Volcanic Complex region. Boletim de Geociencias da Petrobras, 14(1): 143-147.

Viana, A.R. et al., 1998. Hydrology, morphology and sedimentology of the Campos continental margin, offshore Brazil. Sedimentary Geology, 115(1-4): 133-157.

Vieira, P.E., Bruhn, C.H., Santos, C.F., del Rey, A.C. and Alves, R.G., 2007. Golfinho Field-Discovery, development, and future prospects, Offshore Technology Conference, Houston, Texas, 30 April-3 May 2007.

Vincentelli, M.G.C., Possato, S., Mello, M.R. and Contreras, S.A.C., 2007. Análise exploratória integrada da porção noroeste da Bacia do Espírito Santo Mar, 10th International Congress of the Brazilian Geophysical Society, Rio de Janeiro, 19-22, 2007.

Figure captions

Figure 1. a) Regional map of the SE Brazilian margin depicting the location of the Espírito Santo Basin (ESB) and the interpreted seismic volume. **b)** Seafloor time map of the ESB showing the modern Rio Doce channel incising a confined salt-withdrawal basin delimited by N-NW salt ridges and diapirs. D1 to D7: salt diapirs.

Figure 2. a) Regional profile of the Espírito Santo Basin highlighting its main tectono-stratigraphic sequences. Three domains of halokinesis are observed based on salt thickness and structural styles. The study area is located in the transitional domain, which is characterised by the presence of autochthonous salt diapirs. **b)** 3D surface illustrating the morphology of the top salt surface in the study area. Two main salt ridges are observed, with several sub-circular diapirs stemming from N-NE trending salt ridges. Note that the vertical flanks of the diapirs are a surface processing artefact and do not represent true flank morphology.

Figure 3 Seismic profiles depicting the seismo-stratigraphic units and architectural elements interpreted along **a)** E-W (inline) and **b)** N-S (crossline) orientations. In Unit 1, multiple crestal faults are linked to the top of buried salt ridges and synclinal faults occur in the salt-withdrawal basin. Canyon C0 constitutes the main Paleocene sand-prone architectural element in this unit. Unit 2 shows chaotic seismic reflections in heterogeneous MTDs, alternating with continuous high-amplitude reflections comprising turbiditic lobes. The uppermost Unit 3 shows multiple submarine channels and two main submarine canyons. Three sub-units were established based on their channel geometry: sub-unit 3a comprises Canyon C1, sub-unit 3b shows widespread slope incision features in a moderate to low seismic amplitude package, and sub-unit 3c shows

channel features occurring in high-amplitude intervals. MTDs in Unit 3 occur only in sub-unit 3c. The modern Rio Doce Canyon is identified as C2.

Figure 4. a) Maximum amplitude map between horizons Pal1 and H1. High-amplitude features occur within Canyon C0, particularly towards its distal domains. Secondary high-amplitude features are observed close to diapirs D3 and D4, where crestal fault blocks also occur. **b)** Coherence slice taken across Unit 1. Networks of crestal faults occur in the vicinity of both diapir ridges, whereas synclinal faults border canyon C0 along the axis of the basin. Sinuous patterns are observed in distal regions of Canyon C0, and coincide with the higher amplitude features observed in a). **c)** 3D view of a RMS amplitude map computed within a 40 ms time window centred in horizon Pal-1. At this level, high-amplitude features occur close to diapirs and within the main salt-withdrawal basin, which controls the incision of Canyon C0. Crestal faults in the vicinity of the salt ridges and synclinal faults compartmentalise high-amplitude strata. Rose diagrams representing the trend of: **d**) crestal faults on the western salt ridge and **e**) crestal faults on the eastern salt ridge, **f**) synclinal faults, which show a predominance of features striking N-S. These features are intersected by a conjugate (E-W) fault trend.

Figure 5. Data plots of properties of the crestal and synclinal fault sets in Unit 1.

Figure 6. a) Seismic section highlighting amplitude contrasts between MTD-A1 and MTD-A2. Higher amplitudes in MTD-A1 are observed in mass-transport blocks, which often link to underlying faults. MTD-A2 shows a uniform seismic character with high amplitudes and mottled reflections. **b**) Rose diagrams showing identical trends for MTD blocks and crestal faults on the western salt ridge. **c)** RMS amplitude map of MTD-A1 showing multiple mass-transport blocks. **d)** RMS amplitude map of MTD-A2 revealing high-amplitude domains in the salt-withdrawal basin. Irregular features of high amplitude to the east can represent partially deformed blocks.

Figure 7. a) Seismic section highlighting the location and variable lateral extent of interpreted turbidite lobes. Three representative examples are labelled as S1, S2 and S3. **b)**, **c)** and **d)** show amplitude maps within lobes S1, S2 and S3, respectively, evidencing their internal heterogeneities. Elongated high-amplitude features, parallel to the main flow direction of turbidite lobes, are interpreted as intra-lobe conduits with increased homogeneity of coarse-grained (sandy) strata.

Figure 8. a) Profile showing the stratigraphic architecture of Unit 3 in the high confinement area imposed by diapirs D2 and D6. Canyon C1 and C2 are located on the axis of the basin. Channels and incisions in sub-units 3b and 3c are laterally scattered on the continental slope, with higher frequencies towards the western domains. Inset to the lower right-hand side of the figure shows the location of the seismic section. **b)** Two-way Time morphologic map of the erosional envelope of Canyon C1 and **c)** Two-way Time-structural map of Canyon C2 showing its morphology, associated tributaries and confluence points.

Figure 9. a) Channel density map from Gamboa et al. (2012b). Relevant regions with high channel density occur in the salt-withdrawal basin and adjacent to diapirs. Channel density decreases downslope as they coalesce due to topographic confinement. **b)** Coherence slice illustrating the geometry of numerous, partially isolated morphological depressions. The location of this slice is shown in Figure 7a.

Figure 10. a) Log-log plots of width and height (W/H) for architectural elements in the ESB. Two main dimensional classes are present, bounded by the blue and red ellipses, broadly illustrating the ratio contrasts between submarine architectural elements. The larger dimensional class represents relatively unconfined MTDs and turbidite lobes, while the smaller one represents submarine channels constrained by erosional surfaces. **b)** Log-log plot of length and width (L/W) for the interpreted architectural elements. Turbidite lobes constitute the wider features in the graph, standing apart from the remaining elements.

Figure 11. Log-log plots of the average width and height (W/H) for submarine canyons and channels in the ESB. Buried canyon systems show similar average W/H ratios around 12-13. These ratio values were also observed for submarine channels in sub-unit 3c in high confinement areas upslope. Such a character suggest a strong influence of salt structures on these dimensional trends.

Figure 12. Log-log plots illustrating overlapping dimensional ranges for **a**) width/height (W/L) and **b**) length/width (L/W) when considering different architectural elements. The shapes cover the dimensional ranges observed for each data class, and their top and base represent the maximum and minimum aspect ratios observed. Dimensional and ratio overlaps are represented by darker grey colours, highlighting the regions in which two or three distinct classes show identical values.

Table 1. Synthesis table of the H/W (α) and L/W (β) ratios of stratigraphic and structural architectural elements analysed in this paper.

		W=α.H			L=β.W		
		α	α_{Min}	α_{Max}	β	β_{Min}	β_{Max}
Architectural elements	Avg MTD Unit 3	197.0	150.0	290.0			
	Avg MTD Unit 2	250.0	150.0	350.0			
	Turbidites Unit 2	99.6	40.0	310.0	2.9	1.1	7.0
	Canyon C0	11.6	5.0	45.0			
	Canyon C1	12.6	5.0	30.0			
	Canyon C2	4.4	2.0	14.0			
	Avg sub-unit 3b	12.0	10.0	15.0			
	Avg sub-unit 3c	13.0	13.0	18.0			
	sub-unit 3b	10.7	3.0	80.0			
	sub-unit 3c	13.7	3.5	120.0			
	Depressions	10.9	6.0	28.0	1.5	1.0	3.0
	MTD blocks	3.3	1.3	10.0	1.6	1.0	5.0
	Crestal fault compartments				3.1	1.8	5.5
	Synclinal fault compartments				9.6	7.3	17.5

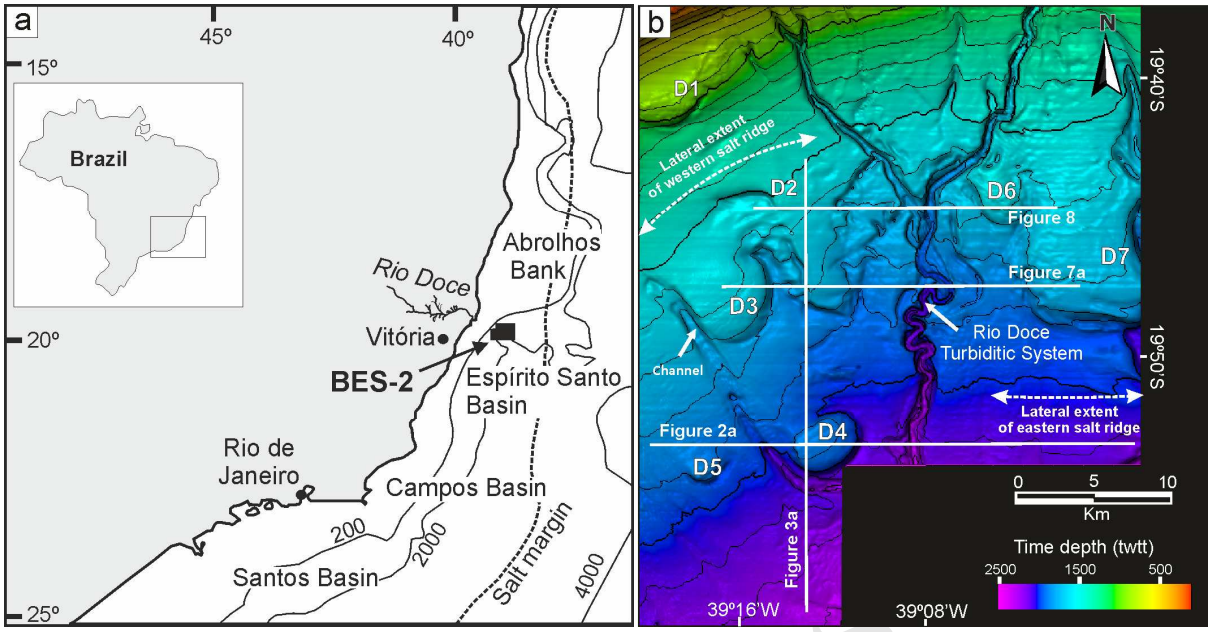

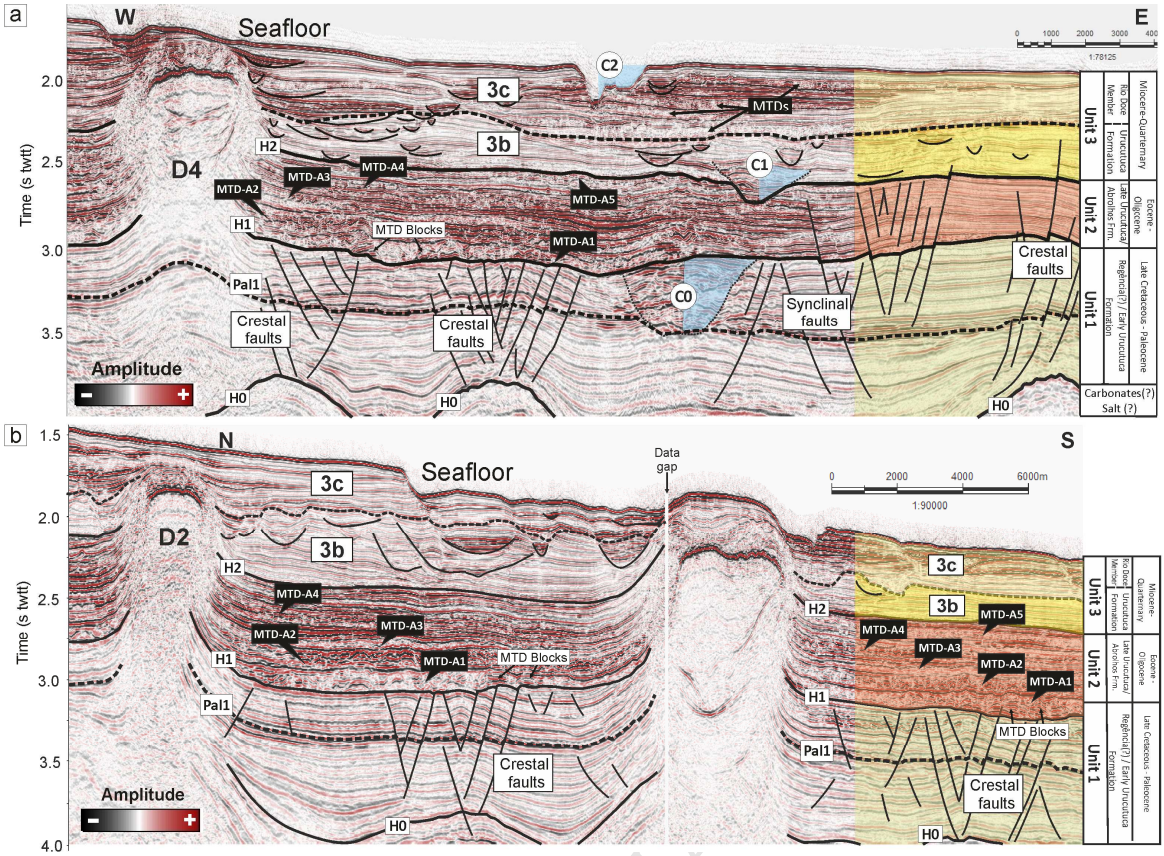

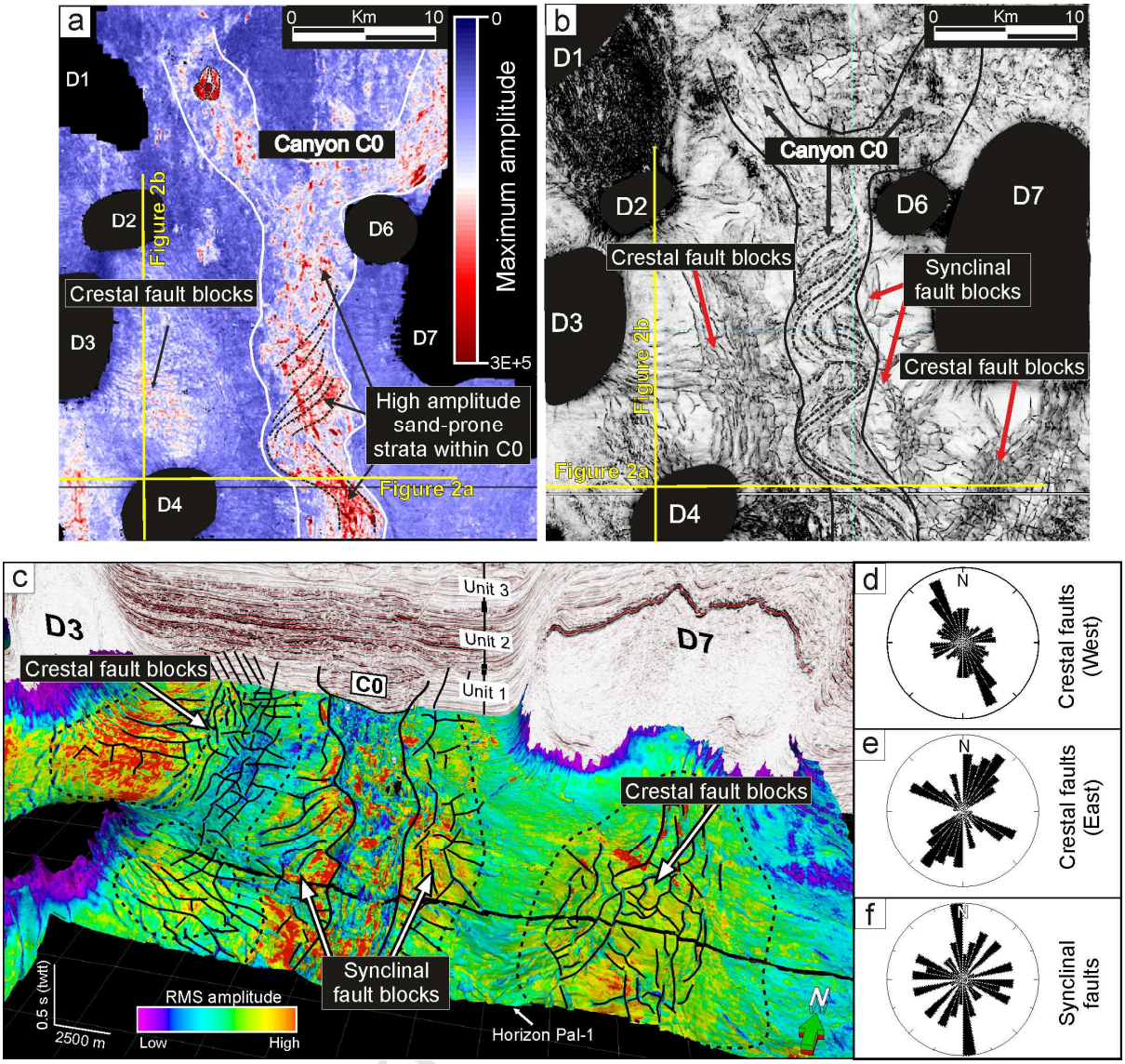
a
0 Km 10
0
Maximum amplitude
3E+5
D1
Canyon C0
Figure 2b
D2
D6
Crestal fault blocks
D3
D7
High amplitude sand-prone strata within C0
Figure 2a
D4
b
0 Km 10
D1
Canyon C0
D2
D6
D7
Crestal fault blocks
Synclinal fault blocks
D3
Figure 2b
Crestal fault blocks
Figure 2a
D4
c
D3
Unit 3
Unit 2
Unit 1
D7
Crestal fault blocks
C0
Crestal fault blocks
Synclinal fault blocks
0.5 s (twtt)
2500 m
RMS amplitude
Low
High
Horizon Pal-1
N
d
N
Crestal faults (West)
e
N
Crestal faults (East)
f
N
Synclinal faults

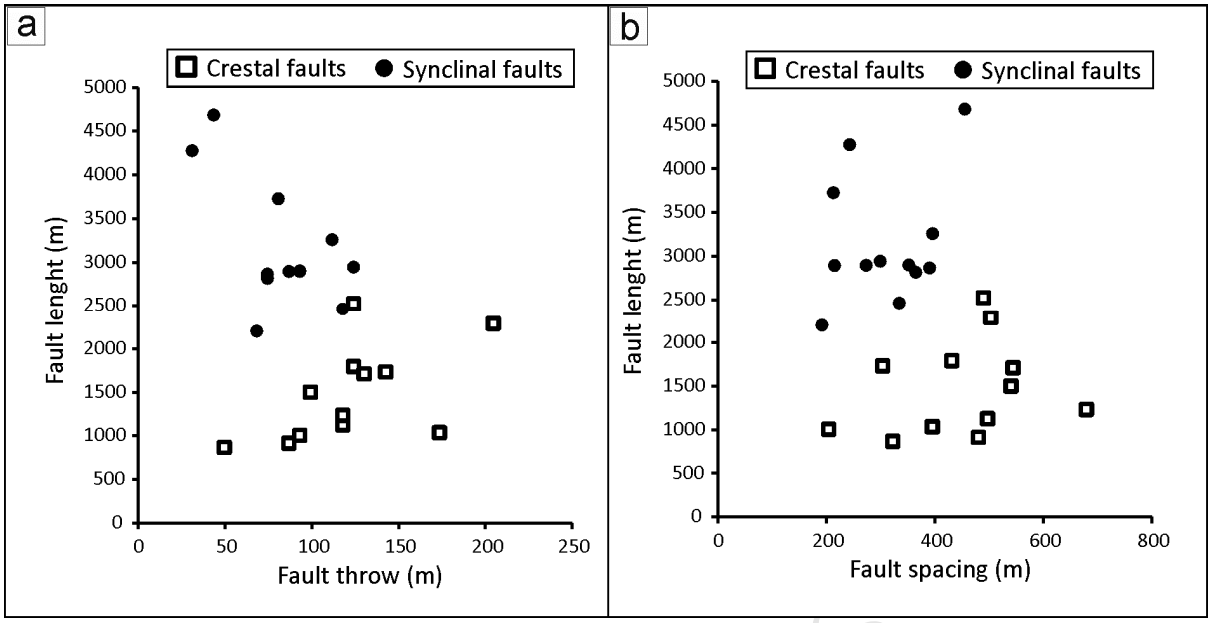

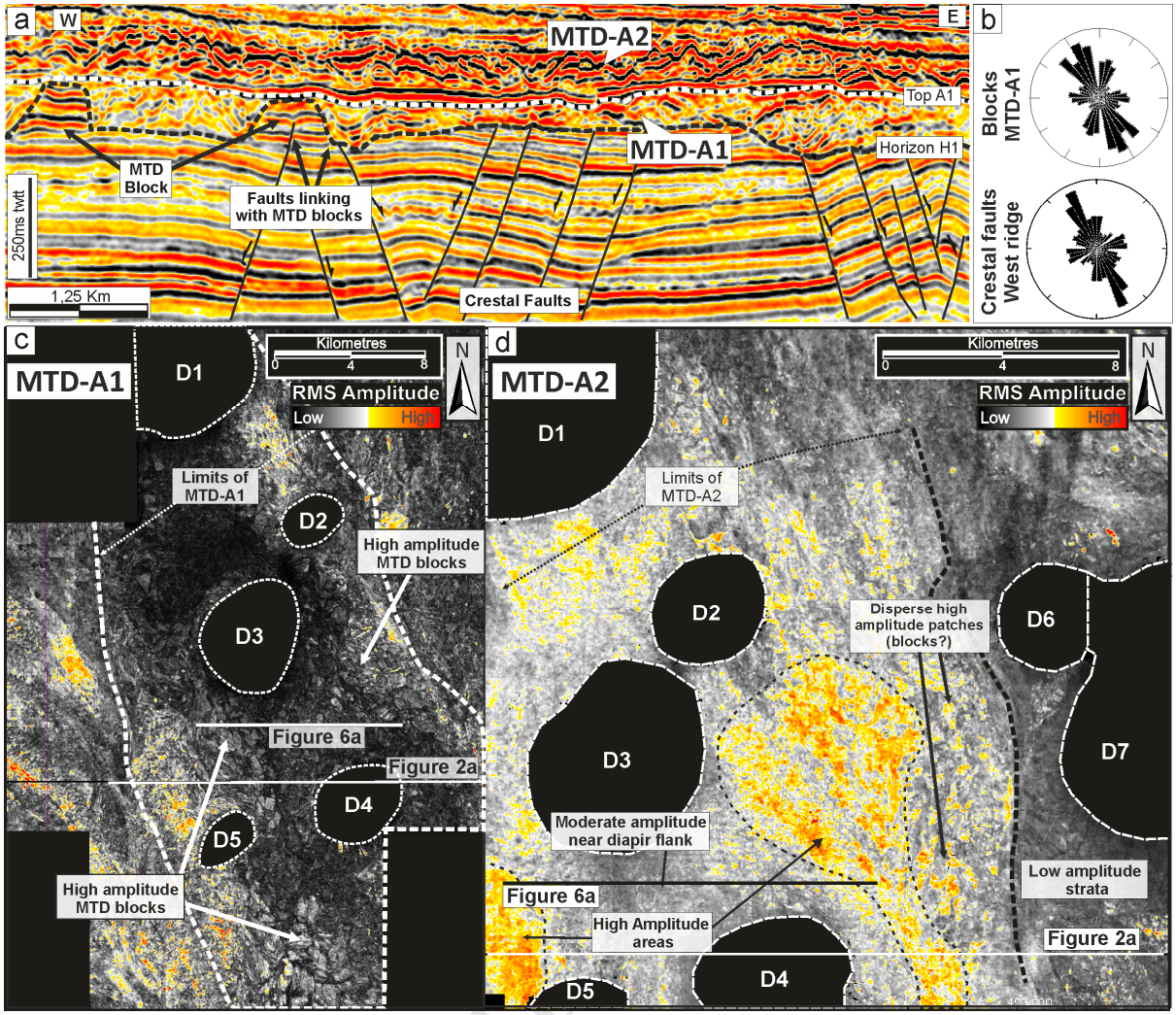

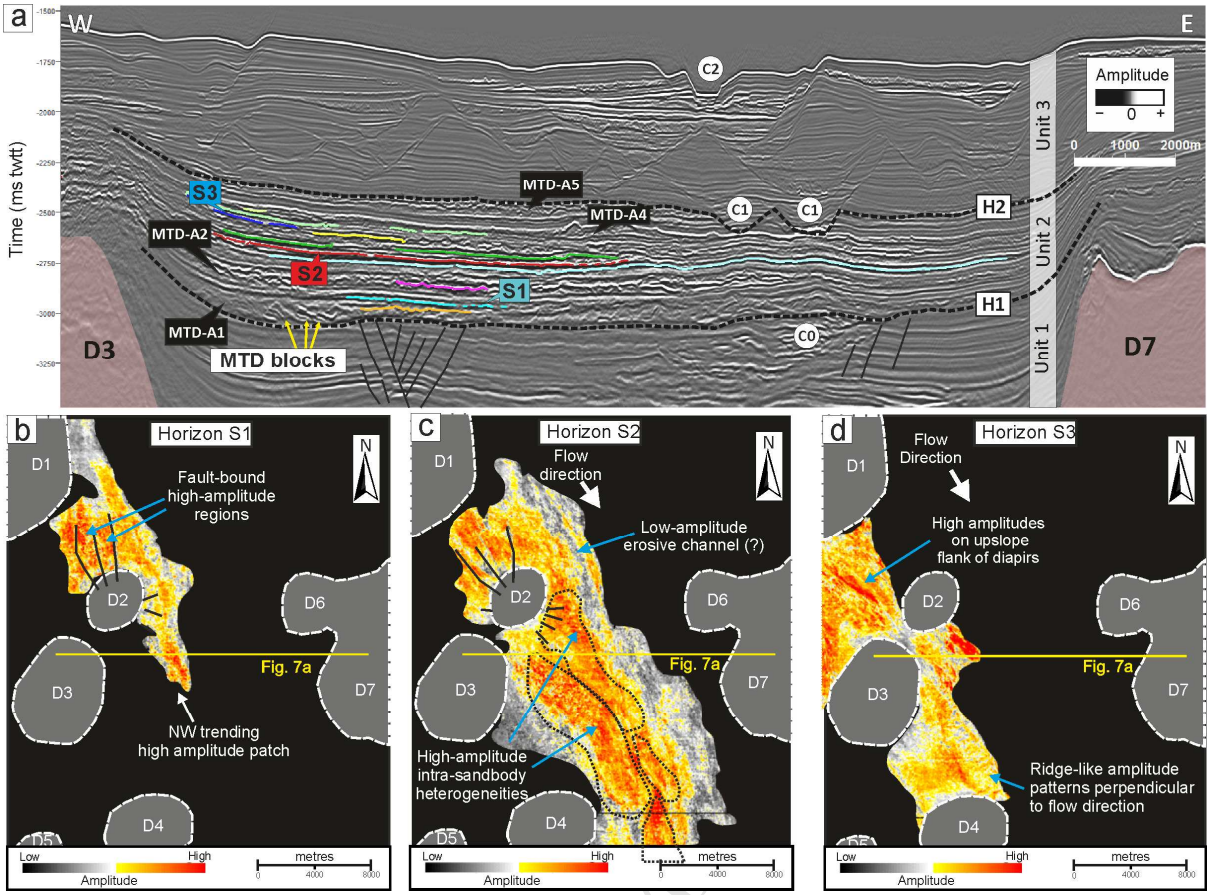

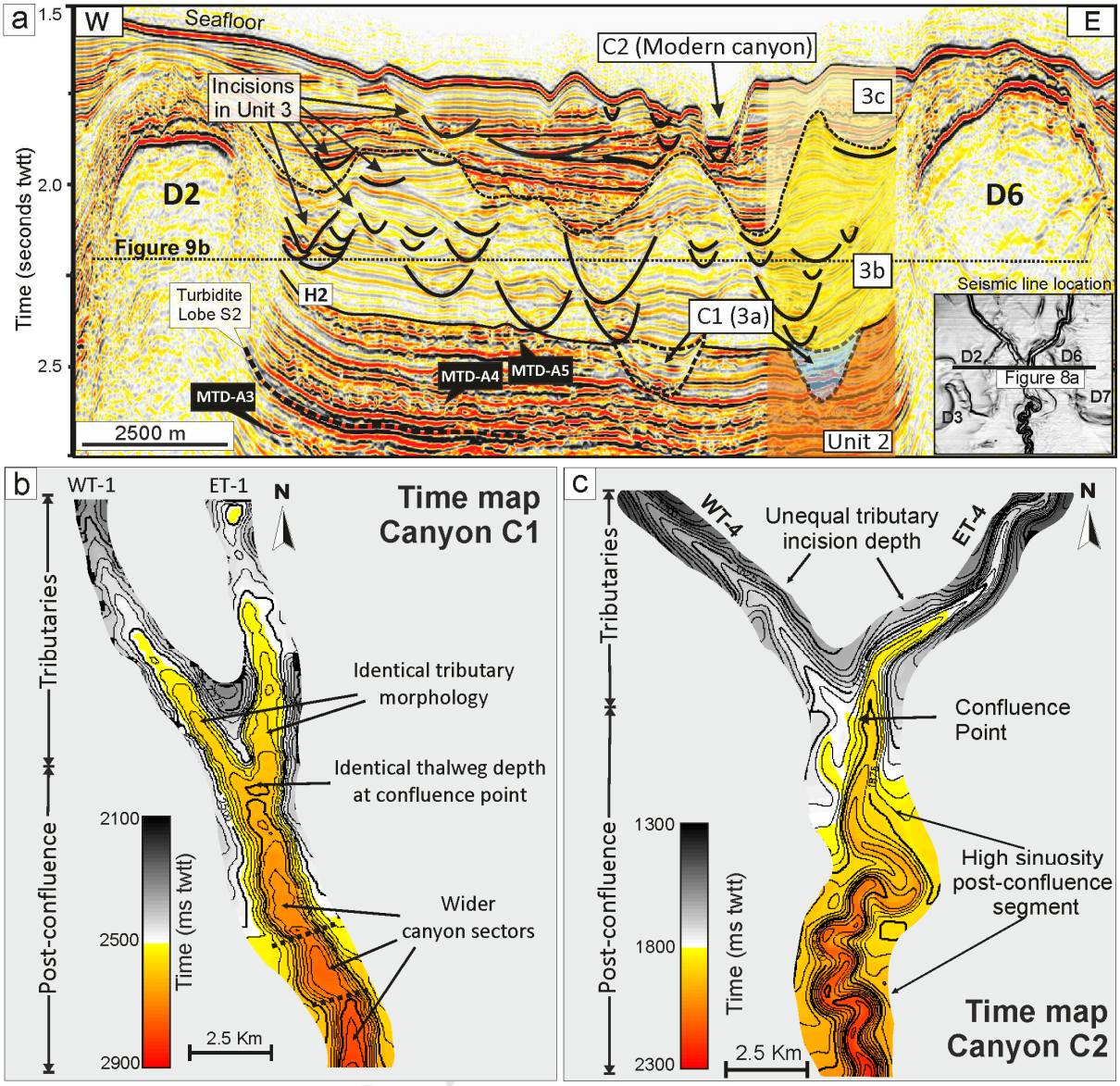
a
W
E
Seafloor
C2 (Modern canyon)
Incisions in Unit 3
3c
D2
D6
Figure 9b
3b
Turbidite Lobe S2
H2
C1 (3a)
MTD-A4
MTD-A5
MTD-A3
2500 m
Unit 2
Seismic line location
D2
D6
Figure 8a
D7
D3
Time (seconds twtt)
1.5
2.0
2.5
b
WT-1
ET-1
N
Time map Canyon C1
Tributaries
Post-confluence
Identical tributary morphology
Identical thalweg depth at confluence point
Wider canyon sectors
2100
2500
2900
Time (ms twtt)
2.5 Km
c
WT-4
ET-4
N
Unequal tributary incision depth
Tributaries
Post-confluence
Confluence Point
High sinuosity post-confluence segment
1300
1800
2300
Time (ms twtt)
2.5 Km
Time map Canyon C2

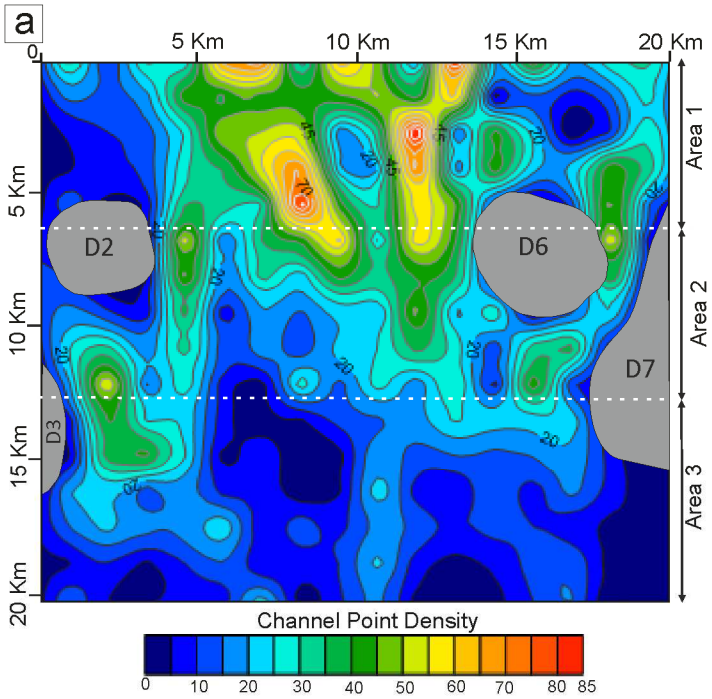

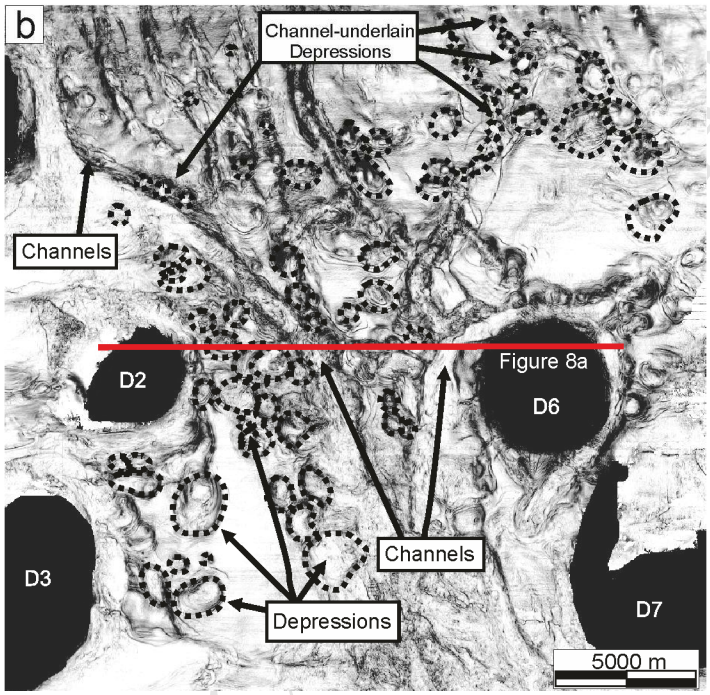

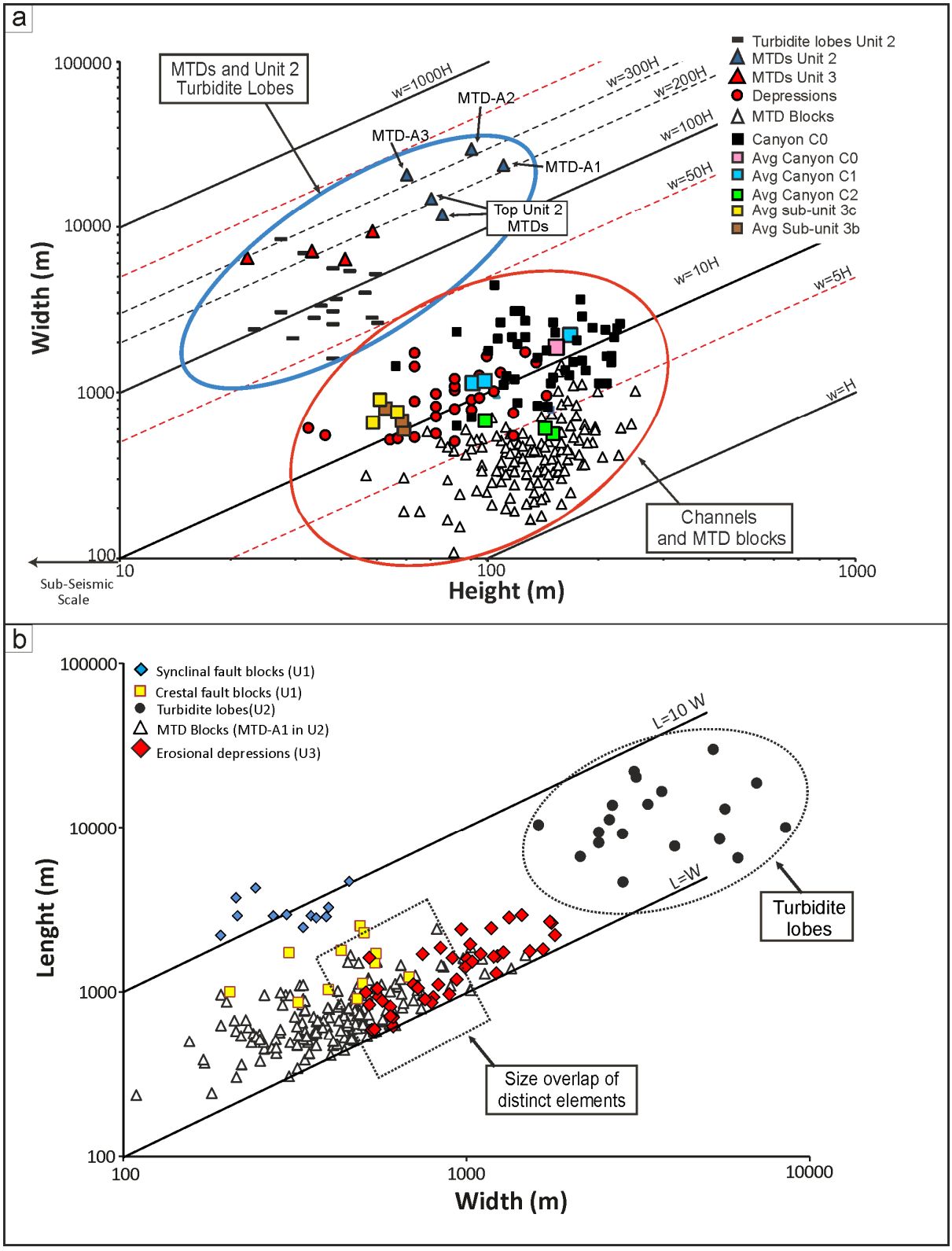
a
MTDs and Unit 2 Turbidite Lobes
MTD-A2
MTD-A3
MTD-A1
Top Unit 2 MTDs
w=1000H
w=300H
w=200H
w=100H
w=50H
w=10H
w=5H
w=H
Channels and MTD blocks
Turbidite lobes Unit 2
MTDs Unit 2
MTDs Unit 3
Depressions
MTD Blocks
Canyon C0
Avg Canyon C0
Avg Canyon C1
Avg Canyon C2
Avg sub-unit 3c
Avg Sub-unit 3b
Width (m)
Height (m)
Sub-Seismic Scale
100000
10000
1000
100
10
100
1000
b
Synclinal fault blocks (U1)
Crestal fault blocks (U1)
Turbidite lobes(U2)
MTD Blocks (MTD-A1 in U2)
Erosional depressions (U3)
L=10 W
L=W
Turbidite lobes
Size overlap of distinct elements
Lenght (m)
Width (m)
100000
10000
1000
100
100
1000
10000

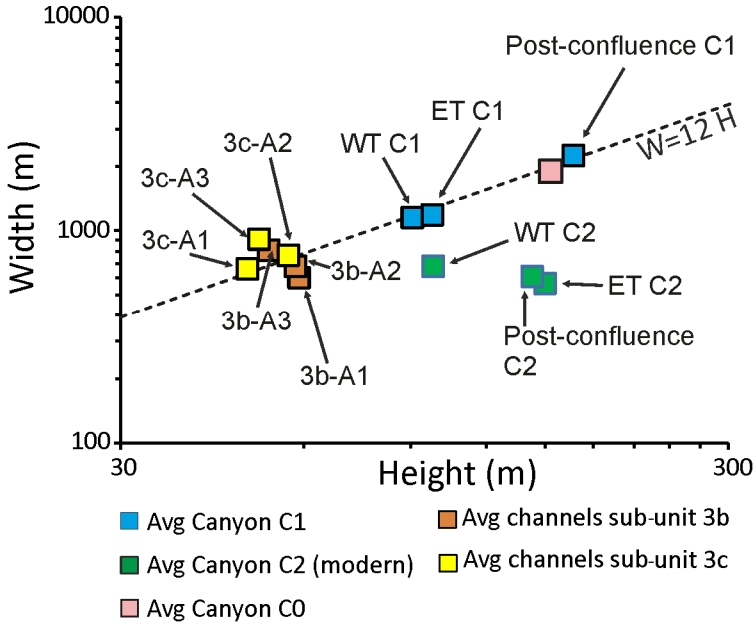

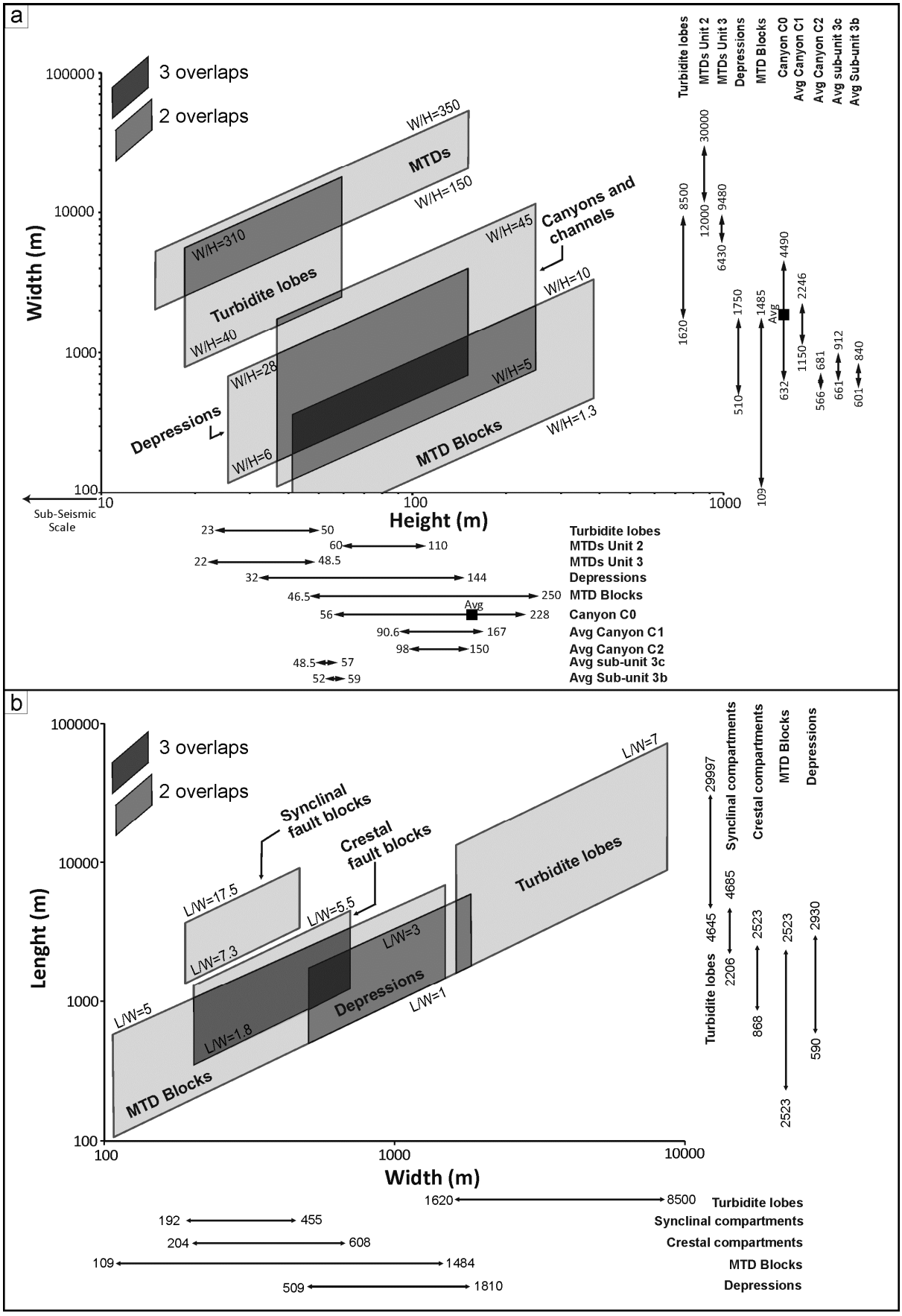
a
3 overlaps
2 overlaps
MTDs
W/H=350
W/H=150
Turbidite lobes
W/H=310
W/H=40
Canyons and channels
W/H=45
W/H=10
Depressions
W/H=28
W/H=6
MTD Blocks
W/H=5
W/H=1.3
Width (m)
Height (m)
Sub-Seismic Scale
100000
10000
1000
100
10
100
1000
Turbidite lobes
MTDs Unit 2
MTDs Unit 3
Depressions
MTD Blocks
Canyon C0
Avg Canyon C1
Avg Canyon C2
Avg sub-unit 3c
Avg Sub-unit 3b
30000
8500
12000
9480
6430
1620
1750
510
1485
109
Avg
4490
2246
1150
632
681
566
912
661
840
601
23 50 Turbidite lobes
60 110 MTDs Unit 2
22 48.5 MTDs Unit 3
32 144 Depressions
46.5 250 MTD Blocks
Avg
56 228 Canyon C0
90.6 167 Avg Canyon C1
98 150 Avg Canyon C2
48.5 57 Avg sub-unit 3c
52 59 Avg Sub-unit 3b
b
3 overlaps
2 overlaps
Synclinal fault blocks
Crestal fault blocks
Turbidite lobes
L/W=7
L/W=17.5
L/W=7.3
L/W=5.5
L/W=3
L/W=5
L/W=1.8
Depressions
L/W=1
MTD Blocks
Lenght (m)
Width (m)
100000
10000
1000
100
100
1000
10000
Synclinal compartments
Crestal compartments
MTD Blocks
Depressions
Turbidite lobes
29997
4645
4685
2206
2523
868
2523
2523
2930
590
1620 8500 Turbidite lobes
192 455 Synclinal compartments
204 608 Crestal compartments
109 1484 MTD Blocks
509 1810 Depressions

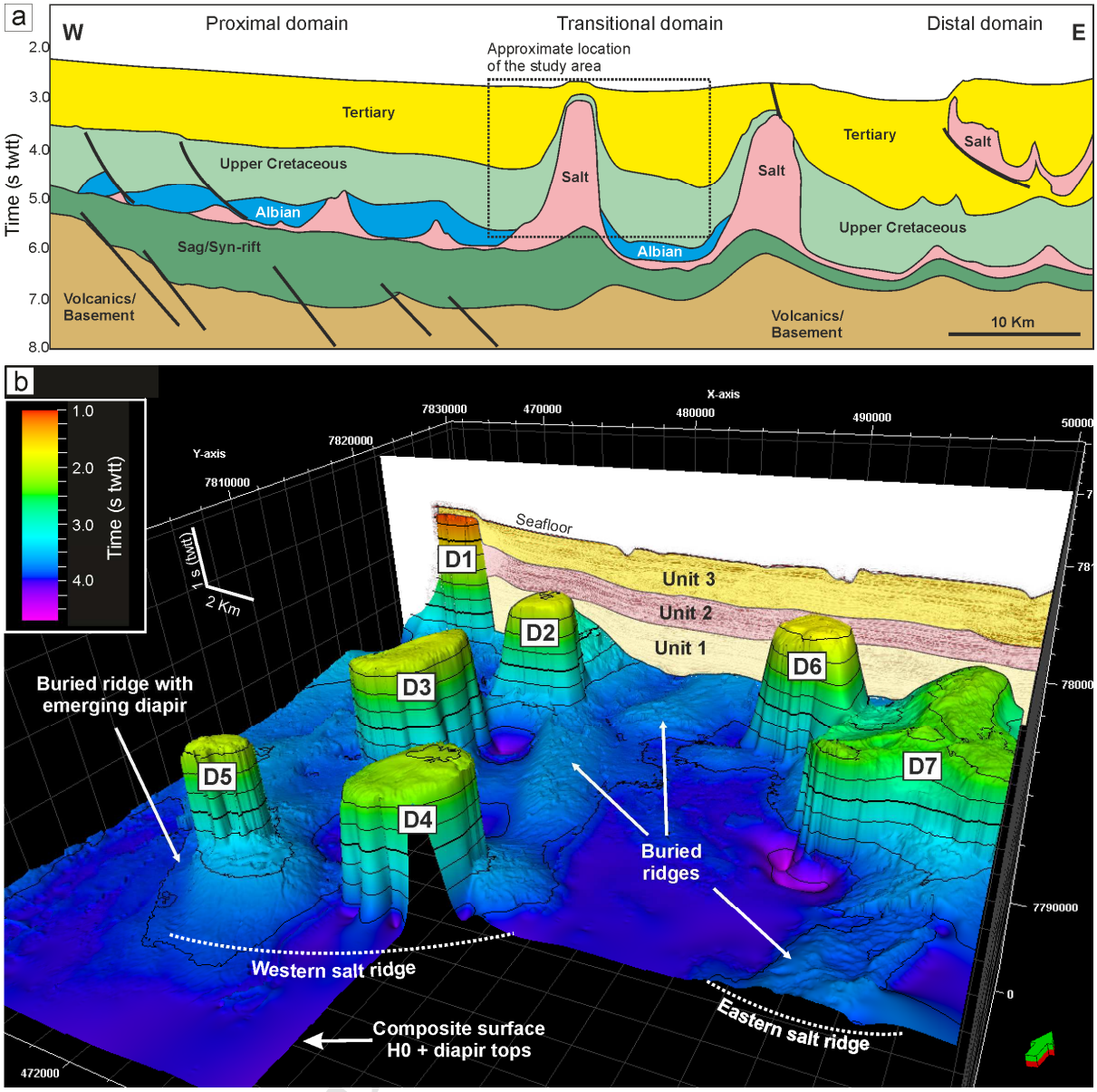

Highlights

> Distinct stratigraphic architectures characterise the Cenozoic units

> Identical scale relationships were observed for distinct architectural elements

> Distribution and dimensions of architectural elements is controlled by salt diapirs

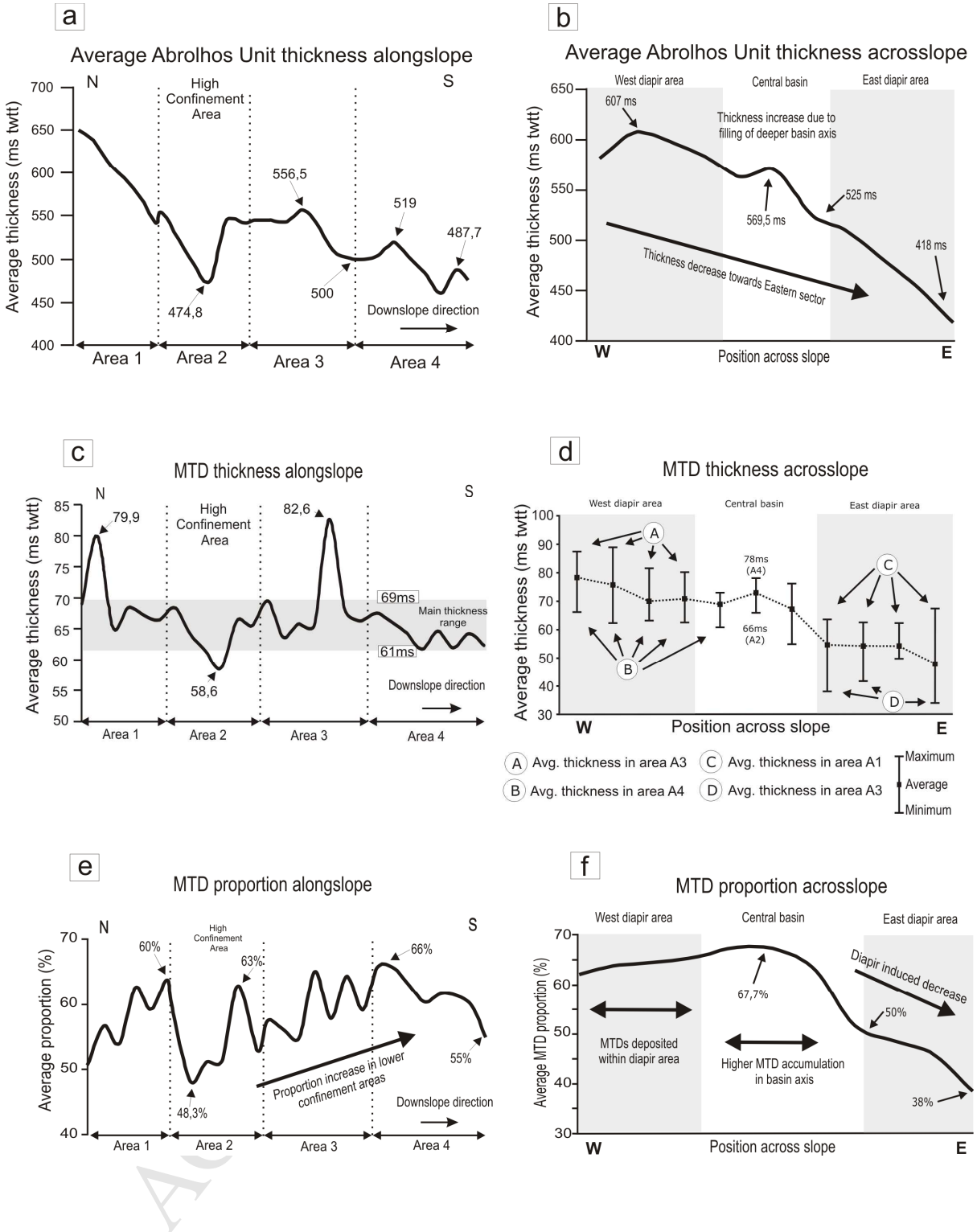
a
Average Abrolhos Unit thickness alongslope
N
S
High Confinement Area
Average thickness (ms twtt)
700
650
600
550
500
450
400
556,5
519
487,7
500
474,8
Downslope direction
Area 1
Area 2
Area 3
Area 4
b
Average Abrolhos Unit thickness acrosslope
West diapir area
Central basin
East diapir area
607 ms
Thickness increase due to filling of deeper basin axis
525 ms
569,5 ms
418 ms
Thickness decrease towards Eastern sector
Average thickness (ms twtt)
650
600
550
500
450
400
W
Position across slope
E
c
MTD thickness alongslope
N
S
High Confinement Area
Average thickness (ms twtt)
85
80
75
70
65
60
55
50
79,9
82,6
69ms
Main thickness range
61ms
58,6
Downslope direction
Area 1
Area 2
Area 3
Area 4
d
MTD thickness acrosslope
West diapir area
Central basin
East diapir area
Average thickness (ms twtt)
100
90
80
70
60
50
40
30
A
B
C
D
78ms (A4)
66ms (A2)
W
Position across slope
E
A Avg. thickness in area A3
B Avg. thickness in area A4
C Avg. thickness in area A1
D Avg. thickness in area A3
Maximum
Average
Minimum
e
MTD proportion alongslope
N
S
High Confinement Area
Average proportion (%)
70
60
50
40
60%
63%
66%
55%
48,3%
Proportion increase in lower confinement areas
Downslope direction
Area 1
Area 2
Area 3
Area 4
f
MTD proportion acrosslope
West diapir area
Central basin
East diapir area
Average MTD proportion (%)
70
60
50
40
30
67,7%
Diapir induced decrease
50%
38%
MTDs deposited within diapir area
Higher MTD accumulation in basin axis
W
Position across slope
E

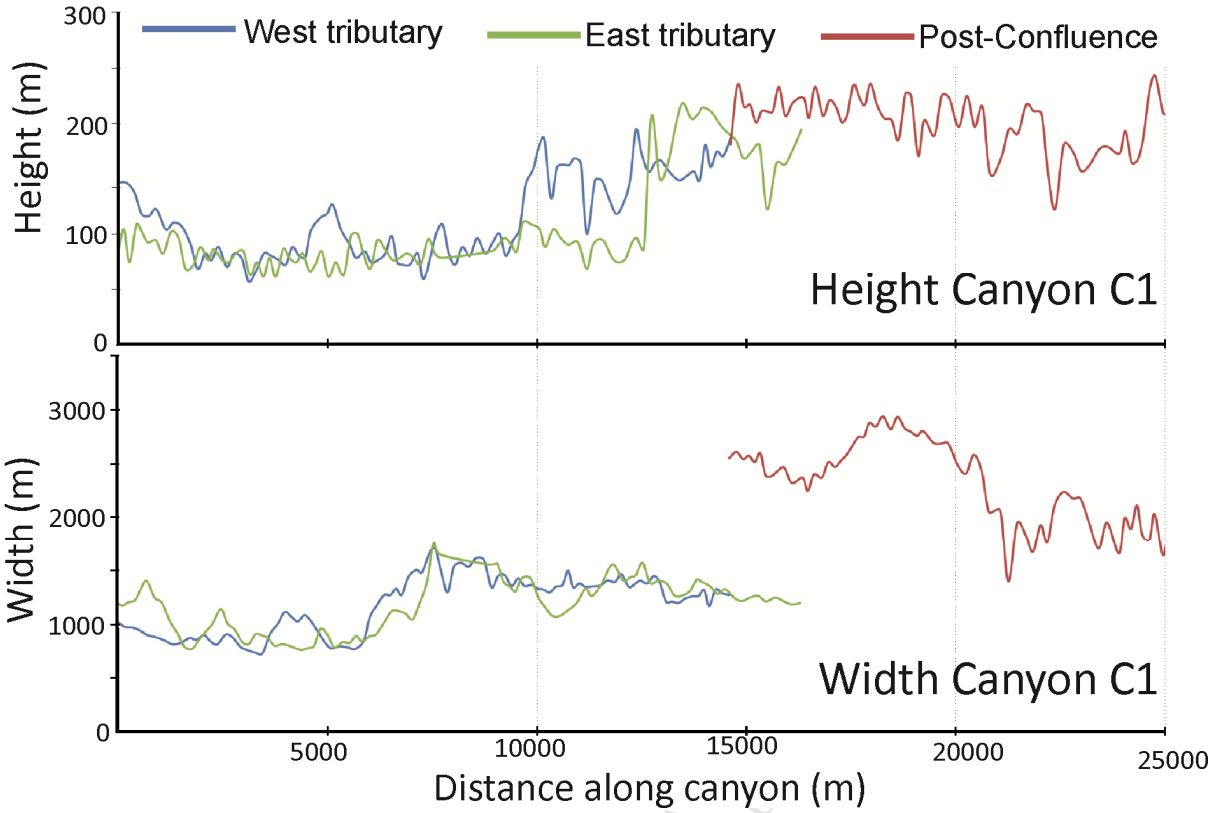

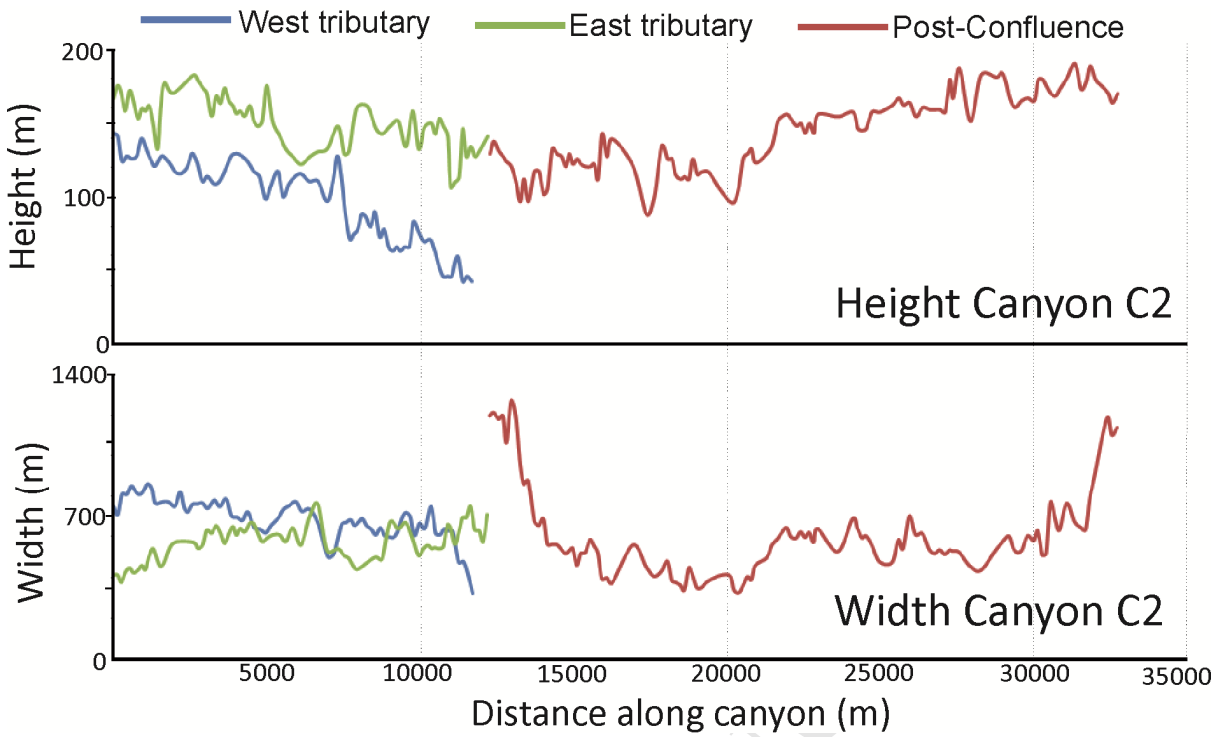

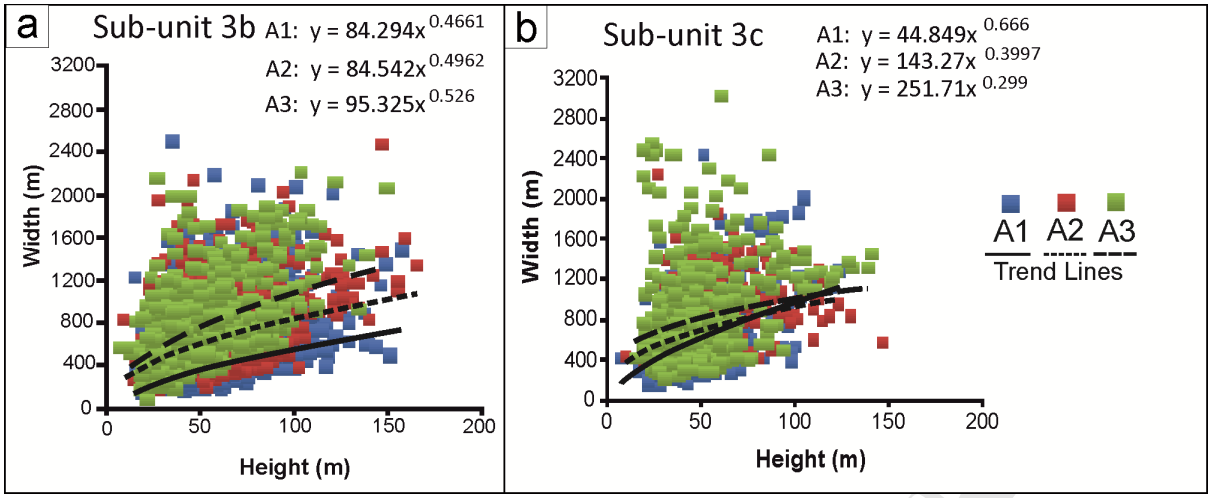

Supplementary material figure captions

Figure S1. Plots representing changes in the thickness and proportion of MTDs in Unit 2. **a** and **b**) Average thickness variations of Unit 2 on the slope. **c** and **d**) Plots showing average MTD thickness variations in Unit 2. The highest accumulations are observed towards the western salt ridge. **e** and **f**) Plots showing the proportion of MTDs in Unit 2 along and across the slope. From Gamboa et al., (2010).

Figure S2. Height and Width measurements of the tributaries and post-confluence segment of Canyon C1. From Gamboa et al. (2012).

Figure S3. Height and Width measurements of the tributaries and post-confluence segment of Canyon C2. From Gamboa et al. (2012).

Figure S4. a) Height and Width measurements of channel features in sub-unit 3b. **b**) Height and Width measurements of channel features in sub-unit 3c. A1, A2 and A3 refer to distinct areas on the slope. From Gamboa et al. (2012).

References for supplementary material:

Gamboa, D., Alves, T., Cartwright, J. and Terrinha, P., 2010. MTD distribution on a 'passive' continental margin: The Espírito Santo Basin (SE Brazil) during the Palaeogene. Marine and Petroleum Geology, 27(7): 1311-1324.

Gamboa, D., Alves, T.M. and Cartwright, J., 2012. A submarine channel confluence classification for topographically confined slopes. Marine and Petroleum Geology, 35(1): 176-189.